THE HEATING OF SOLAR CORONAL LOOPS BY ALFVÉN WAVE TURBULENCE

A. A. van Ballegooijen,[1] M. Asgari-Targhi,[2] and A. Voss[3, 2]

[1] 5001 Riverwood Avenue, Sarasota, FL 34231, USA
[2] Harvard-Smithsonian Center for Astrophysics, 60 Garden Street, Cambridge, MA 02138, USA
[3] School of Computer Science, University of St Andrews, Jack Cole Building, North Haugh, St Andrews, Fife, KY16 9SX, Scotland, UK

ABSTRACT

In this paper we further develop a model for the heating of coronal loops by Alfvén wave turbulence (AWT). The Alfvén waves are assumed to be launched from a collection of kilogauss flux tubes in the photosphere at the two ends of the loop. Using a three-dimensional magneto-hydrodynamic (MHD) model for an active-region loop, we investigate how the waves from neighboring flux tubes interact in the chromosphere and corona. For a particular combination of model parameters we find that AWT can produce enough heat to maintain a peak temperature of about 2.5 MK, somewhat lower than the temperatures of $3 - 4$ MK observed in the cores of active regions. The heating rates vary strongly in space and time, but the simulated heating events have durations less than 1 minute and are unlikely to reproduce the observed broad Differential Emission Measure distributions of active regions. The simulated spectral line non-thermal widths are predicted to be about 27 km s^{-1}, which is high compared to the observed values. Therefore, the present AWT model does not satisfy the observational constraints. An alternative "magnetic braiding" model is considered in which the coronal field lines are subject to slow random footpoint motions, but we find that such long period motions produce much less heating than the shorter period waves launched within the flux tubes. We discuss several possibilities for resolving the problem of producing sufficiently hot loops in active regions.

1. INTRODUCTION

The nature of coronal heating is one of the unsolved problems in solar physics (see reviews by Zirker 1993; Schrijver & Zwaan 2000; Aschwanden 2005; Klimchuk 2006; De Moortel & Browning 2015). The energy for coronal heating is believed to originate in the convection zone below the photosphere, but the details of how this energy is transported to and dissipated in the corona are not well understood. One possibility for heating coronal loops is that the sub-surface convective flows cause twisting and braiding of coronal field lines, which leads to the formation of thin current sheets in the corona where magnetic reconnection can take place (e.g. Parker 1972, 1983; Berger 1991, 1993; Priest et al. 2002; Janse et al. 2010; Berger et al. 2015; Wilmot-Smith 2015; Pontin & Hornig 2015; Pontin et al. 2017). The reconnection likely proceeds in a burst-like manner, producing "nanoflares" (Parker 1988), and the corona may be heated by the combined effect of a large number of such nanoflares occurring at different times and positions within the coronal loop (e.g., Cargill 1994; Klimchuk 2010; Cargill et al. 2015). The strongest heating occurs in active regions, which have broad temperature distributions with temperatures in the range 1 to 6 MK (e.g., Kano & Tsuneta 1996; Winebarger et al. 2011; Warren et al. 2011, 2012; DelZanna et al. 2015b). In the nanoflare model these broad temperature distributions are explained by assuming that an observed coronal loop consist of multiple threads, each in a different state of its temperature evolution (Cargill & Klimchuk 1997, 2004; Patsourakos & Klimchuk 2009; Cargill et al. 2015; López-Fuentes & Klimchuk 2015). Coronal radio bursts may be a signature of nanoflare heating (Mercier & Trottet 1997). Ohmic dissipation of braided magnetic fields is assumed to be the main cause of coronal heating in MHD models of coronal loops (e.g., Rappazzo et al. 2007, 2008; Dahlburg et al. 2016) and entire active regions (e.g., Gudiksen & Nordlund 2005; Bingert & Peter 2011; Bourdin et al. 2015).

In the photosphere outside sunspots the magnetic field is highly intermittent and is concentrated in small magnetic flux elements ("flux tubes"), which have kilogauss field strengths and widths of a few 100 km or less (e.g., Stenflo 1973; Solanki 1993; Berger & Title 1996, 2001). These flux tubes may be formed by convective collapse (Parker 1978; Spruit 1979; Nagata et al. 2008; Fischer et al. 2009). In plage regions the magnetic flux concentrations have typical field strengths of about 1500 G, and the flux tubes expand with height (Martínez Pillet et al. 1997; Berger et al. 2004; Buehler et al. 2015). Strong downflows occur in the immediate surroundings of these flux tubes. Neighboring flux tubes merge at some height in the upper photosphere or low chromosphere (e.g., Bruls & Solanki 1995). Transverse MHD waves can be produced in such flux tubes as a result of their interactions with granule-scale convective flows (e.g., Matsumoto & Shibata 2010; Mumford et al. 2015). Such waves may propagate upward into the solar atmosphere and dissipate their energy in the corona (Alfvén 1947; Wentzel 1974; Hollweg 1978; Parnell & De Moortel 2012; Arregui 2015; Cranmer et al. 2015). Alfvén waves are of particular interest because they can propagate over large distances in the corona before giving up their energy. Transverse waves have been observed in the corona above the solar limb (Tomczyk et al. 2007; Tomczyk & McIntosh 2009; Threlfall et al. 2013; Morton et al. 2015), in the swaying motions of spicules (De Pontieu et al. 2007), in network jets on the solar disk (Tian et al. 2011, 2014), and in the solar wind (Coleman 1968; Belcher 1971; Matthaeus et al. 1990; Bale et al. 2005; Borovsky 2012). The observed amplitudes of Alfvén waves at the coronal base are sufficient to heat and accelerate the solar wind (De Pontieu et al. 2007; McIntosh et al. 2011), and Alfvén waves are believed to be the main driver of the fast wind (e.g., Suzuki & Inutsuka 2005; Cranmer et al. 2007; Verdini & Velli 2007; Chandran et al. 2011). Alfvén waves may also be responsible

for heating coronal loops (e.g., Moriyasu et al. 2004; Antolin & Shibata 2010; van Ballegooijen et al. 2011, hereafter paper I). These models assume that the waves originate in the photosphere, not as a by-product of nanoflares in the corona. Therefore, the connection to the photosphere is very important in wave heating models.

There are many observational constraints on coronal heating models. First and foremost, the model should reproduce the observed coronal temperatures and densities (e.g., Winebarger et al. 2011; Warren et al. 2011, 2012), as well as the spatial and temporal variations of these quantities (e.g., Viall & Klimchuk 2011, 2012). Many coronal loops seen in EUV and X-ray images have nearly constant cross-sections (e.g., Klimchuk 2000; López-Fuentes et al. 2006, 2008), which appears to be in conflict with the basic idea that the magnetic field lines expand with height in the corona. Observations of the "moss" at the ends of hot loops provide constraints on the energy losses by downward conduction (Fletcher & de Pontieu 1999; Martens et al. 2000; Warren et al. 2008; Winebarger et al. 2011), and measurements of plasma density can provide constraints on the spatial distribution of the heating (Fludra et al. 2017). Second, the model should reproduce the observed spectral line widths, which are broadened in excess of their thermal widths (e.g., Doschek et al. 2007; Young et al. 2007; Tripathi et al. 2009; Warren et al. 2011; Tripathi et al. 2011; Tian et al. 2011, 2012a,b; Doschek 2012; Brooks & Warren 2016; Testa et al. 2016). The observed non-thermal broadening provides constraints on unresolved reconnection outflows in the corona, and on the velocity amplitudes of MHD waves. Third, the model should be consistent with observations of the braiding or twisting of the coronal field lines, or the lack thereof (e.g., Schrijver et al. 1999; Brooks et al. 2013). Finally, the model should explain observations of coronal "rain" (e.g., Antolin & Rouppe van der Voort 2012; Antolin et al. 2015), which provide information on the heating and cooling of the coronal plasma.

Another, often overlooked constraint comes from observations of the motions of magnetic flux elements in the photosphere (e.g., Muller et al. 1994; Schrijver et al. 1996; Berger & Title 1996, 2001; Berger et al. 1998; van Ballegooijen et al. 1998; Manso Sainz et al. 2011; Wedemeyer-Böhm et al. 2012). Such horizontal motions are believed to be responsible for the braiding of coronal magnetic field lines (Parker 1972, 1983) and/or the generation of transverse MHD waves (Vigeesh et al. 2012; Mumford et al. 2015). Photospheric "bright points" are often used as proxies for kilogauss flux elements (e.g., Berger & Title 1996; Nisenson et al. 2003; Abramenko et al. 2011; Utz et al. 2010). Chitta et al. (2012) used high-cadence observations of isolated bright points and measured an rms velocity $v_{\rm rms} = 1$ km s^{-1} and a velocity autocorrelation time $\tau_{\rm c} = 30$ s, but this represents only the motions on very short time scales. On longer time scales the random motions are often characterized as "random walk" with a certain photospheric diffusion constant D. In magnetic network and plage regions $D \approx 60$ km^2 s^{-1} on a time scale of a few thousand seconds (Berger et al. 1998), and on a time scale of several days D is in the range $100 - 250$ km^2 s^{-1} (DeVore et al. 1985; Wang 1988; Schrijver & Martin 1990; Komm et al. 1995; Schrijver et al. 1996; Hagenaar et al. 1999). These values of D put severe constraints on the rate at which magnetic energy can be injected into the corona by random footpoints motions (van Ballegooijen 1986, and paper I).

In this paper we focus on the wave heating model, but we also compare it with the magnetic braiding model. In paper I only a single magnetic flux tube was considered, so the interactions between neighboring flux tubes were ignored. In contrast, in magnetic braiding models the different flux tubes are assumed to be wrapped around each other by photospheric convective flows, and thin current sheets are expected to develop at the interfaces between the flux tubes (e.g., Parker 1983;

Wilmot-Smith et al. 2009; Rappazzo et al. 2013; Pontin & Hornig 2015; Richie et al. 2016). It is desirable to include the effects of multiple flux tubes also in the wave heating models. Here we extend the model of paper I to include the interactions between neighboring flux tubes. We investigate how the transverse waves from neighboring flux tubes interact in the chromosphere and corona. Current sheets can develop at the boundaries between the tubes because the tangential component of velocity is not expected to be continuous across such boundaries for waves originating in different flux tubes. The dissipation of these boundary currents may increase the wave heating compared to models with a single flux tube. We also make further improvements to the treatment of the chromosphere-corona transition regions (TRs) at the two ends of the coronal loop. In paper I the TRs were treated as discontinuities in plasma density, and their effect on the Alfvén waves was described in terms of reflection and transmission coefficients. In the present work the TRs are fully resolved along the loop.

The paper is organized as follows. Previous work on the wave heating model is summarized in section 2. In section 3 we describe a new wave heating model for coronal loops in which the magnetic field of the loop is anchored in a collection of kilogauss flux tubes in the photosphere. The model describes the dynamics of Alfvén waves in such a complex magnetic structure. In section 4 simulation results are presented for one particular set of model parameters. We study the spatial distribution of the heating, the amplitude of heating events at various positions along the loop, and the effects of the waves on spectral line profiles. In section 5 we consider a magnetic braiding model in which the photospheric flux tubes are omitted and the footpoint motions occur on longer time scales, but with exactly the same background atmosphere as the first model. Therefore, the heating rates predicted by the two models can be directly compared. We find that for the same velocity of footpoint motions (about 1 km s^{-1}) the magnetic braiding model produces less heating than the wave heating model. The results are further discussed in section 6.

2. WAVE HEATING MODELS

Transverse MHD waves can be dissipated in a variety of ways. In the presence of density variations across the magnetic field lines, the waves can be damped by phase mixing and resonant absorption, which cause wave energy to be transferred to smaller scales (Heyvaerts & Priest 1983; Poedts et al. 1990; De Groof & Goossens 2002; Goossens et al. 2011, 2012, 2013; Pascoe et al. 2011, 2012). Torsional Alfvén waves can interact nonlinearly with the background plasma to produce parallel flows and shocks, which provide another dissipation channel (Kudoh & Shibata 1999; Moriyasu et al. 2004; Suzuki & Inutsuka 2005; Antolin & Shibata 2010). Counter-propagating Alfvén waves are subject to nonlinear interactions (Iroshnikov 1963; Kraichnan 1965), which produce turbulent cascades (e.g., Shebalin et al. 1983; Goldreich & Sridhar 1995; Maron & Goldreich 2001; Cho et al. 2002). The resulting Alfvén wave turbulence (AWT) is believed to play an important role in the heating of the corona in both open and closed magnetic structures (Matthaeus et al. 1999; Oughton et al. 2001; Dmitruk & Matthaeus 2003).

A key feature of AWT in a low-beta plasma is that it is highly anisotropic, with velocity perturbations nearly perpendicular to the background magnetic field, and with perpendicular length scales much smaller than the parallel ones. Therefore, AWT in the solar corona is expected to be quite different from isotropic turbulence in ordinary fluids. Strong AWT can develop even when the velocity amplitude $\delta v_\perp$ of the counter-propagating waves is much smaller than the Alfvén speed ($\delta v_\perp \ll v_A$). Reflection-driven AWT is believed to be responsible for producing the fast solar wind (e.g., Cranmer

et al. 2007; Verdini & Velli 2007; Chandran et al. 2011). Detailed 3D MHD simulations of turbulent waves in the acceleration region of the solar wind have been described by Perez & Chandran (2013) and van Ballegooijen & Asgari-Targhi (2016, 2017, hereafter paper V). Density variations across the magnetic field are known to exist both in coronal loops and in the solar wind. Most turbulence modeling is based on the reduced MHD approximation (Strauss 1976, 1997), which produces a passive cascade of density and magnetic-field-strength fluctuations at scales larger than the ion-gyro radius (e.g., Schekochihin et al. 2009). However, most solar models developed so far neglect the density fluctuations altogether (e.g., Perez & Chandran 2013, papers I and IV). Therefore, the turbulence models do not yet include the important effects of phase mixing and resonant absorption. Conversely, most studies of resonant absorption use linearized versions of the MHD equations, and therefore neglect the effect of the waves on the background density variations, as well as the nonlinear couplings between counter-propagating transverse waves. Therefore, a comprehensive description of the physical processes that cause wave energy to be transferred to smaller scales is not yet available.

Alfvén wave turbulence may also be responsible for the heating of the chromosphere and corona in active regions (paper I). Alfvén- and kink waves can be produced in photospheric flux tubes as a result of their interactions with granule-scale convective flows (e.g., Mumford et al. 2015). In paper I we treated the flux tubes as having rigid walls, so the transverse waves could be approximated as Alfvén waves and simulated using the reduced MHD approximation. We found that the waves propagate upward along the expanding flux tube and reflect due to variations in Alfvén speed with height; this led to the development of AWT in both the chromospheric and coronal parts of the loop. In the corona the counter-propagating waves are launched from both ends of the loop, so they have roughly equal amplitudes and their nonlinear interactions are quite strong. It was found that the loops typically observed in active regions can be explained in terms of AWT, provided the small-scale footpoint motions in the photosphere have velocities of $1 - 2$ km s^{-1} and time scales of $60 - 200$ s.

Magnetic braiding does occur in the AWT model, but the braids are highly dynamic and not close to a force-free state. This is a consequence of the fact that the lower atmosphere is included in the model. The high density of the photosphere compared to the corona implies that all perturbations tend to be wave-like, and quasi-static evolution is found only when the lower atmosphere is omitted from the modeling (van Ballegooijen et al. 2014). Another key feature of the AWT model is that the energy injected into the corona is dissipated on a time scale comparable to the coronal Alfvén travel time, which is $20 - 60$ s for typical active-region loops. In contrast, in the nanoflare model it is assumed that magnetic free energy can be built up in the corona for thousands of seconds before part of the energy is released in a reconnection event. This requires that the current layers in the corona maintain a finite thickness, so that reconnection does not occur prematurely and energy can build up over a longer period of time (e.g., Wilmot-Smith et al. 2009; Pontin & Hornig 2015; Richie et al. 2016). Whether such energy build-up occurs or not depends on the nature of the magnetic structures and flows in the lower atmosphere where convective driving takes place. Therefore, it is important to include the lower atmosphere in models for coronal heating.

The AWT model was further developed by constructing loop models for active regions observed with the *Solar Dynamics Observatory* (Asgari-Targhi & van Ballegooijen 2012; Asgari-Targhi et al. 2013, 2014, hereafter papers II, III and IV). Papers II and IV used nonlinear force-free field (NLFFF) modeling to obtain the magnetic field strength $B_0(s)$ as a function of position s along the loops, which is a key parameter in any heating model; paper III used potential-field modeling. A set of

field lines was selected, and for each one the wave turbulence in a thin flux tube surrounding the selected field line was simulated. It was found that the wave heating rate $Q(s,t)$ averaged over the loop cross-section depends on the position along the loop, and varies with time in a burst-like manner. The mean heating rate $\overline{Q}$ averaged over the coronal volume and over time was about 10^{-3} erg cm^{-3} s^{-1}, but the peak rates during heating events was about one order of magnitude larger. The peak temperature T_{max} in the different loops was predicted to be in the range 2.1 - 2.9 MK, but for any given loop the model predicts only small temperature variations, $\Delta T \sim 0.1$ MK. This is due to the modest amplitude of the heating events, and the fact that they are localized along the loop, so that their effect is quickly diminished by thermal conduction. Therefore, in its present form the AWT model cannot explain the higher temperatures of 4 - 6 MK observed in many active regions. The higher temperatures can be obtained only by increasing the footpoint velocities to about $5-6$ km s^{-1} (Asgari-Targhi et al. 2015), which seems beyond what may be expected for magnetic footpoint motions in the photosphere on small spatial scales.

Paper IV used the Extreme-ultraviolet Imaging Spectrometer (EIS) on *Hinode* to derive observational constraints on Alfvén wave amplitudes at the loop tops for an active region observed on 2012 September 7. Spectral lines of Fe XII, Fe XIII, Fe XV and Fe XVI were used to derive non-thermal velocities from the observed line widths. The authors found wave amplitudes in the range $20-34$ km s^{-1} for the Fe XII 192 Å line, consistent with predictions from the AWT model. However, we now realize that the instrumental line width may have been underestimated, so the non-thermal velocities may have been overestimated. More complete EIS observations were presented by Brooks & Warren (2016), who measured non-thermal line widths in 15 non-flaring active regions and found a mean value of 17.6 ± 5.3 km s^{-1}. Also, Testa et al. (2016) used the Interface Region Imaging Spectrometer (IRIS) and found modest non-thermal velocities with an average of about 24 km s^{-1} and a peak of the velocity distribution at 15 km s^{-1}. Hara & Ichimoto (1999) used a coronagraph and spectrometer at the Norikura Solar Observatory to place constraints on the amplitudes of Alfvén waves in an active region observed above the solar limb (also see Ichimoto et al. 1995). They found that the non-thermal velocities for Fe X 6374 Å, Fe XIV 5303 Å and Ca XV 5694 Å are in the ranges $14-20$, $10-18$, and $16-26$ km s^{-1}, respectively. These observations of non-thermal velocity put severe constraints on the AWT model for coronal heating.

In the above-mentioned works only a single magnetic flux tube was considered, corresponding to one kilogauss flux element in the photosphere (magnetic flux $\Phi = 4.4 \times 10^{17}$ Mx). Therefore, we implicitly assumed that a photospheric flux tube at one end of the coronal loop is connected to a single flux tube at the other end. In reality the photospheric flux elements at the two ends of a loop are uncorrelated and do not perfectly match up. In the next section we develop a somewhat more realistic model containing multiple flux tubes that are not co-aligned at the two ends.

3. CORONAL LOOP MODEL CONTAINING MULTIPLE FLUX TUBES

3.1. *Lower Atmosphere*

Coronal loops in active regions are anchored in the photosphere. The magnetic field in the photosphere is highly intermittent and consists of a collection of kilogauss flux concentrations separated by areas with much weaker fields (e.g., Buehler et al. 2015). In this paper we use a very simplified model for the photospheric flux tubes, in which the tubes have square cross-sections and are located on a square lattice, as illustrated in Figure 1. An array of 4×4 flux tubes is considered. Figure 1
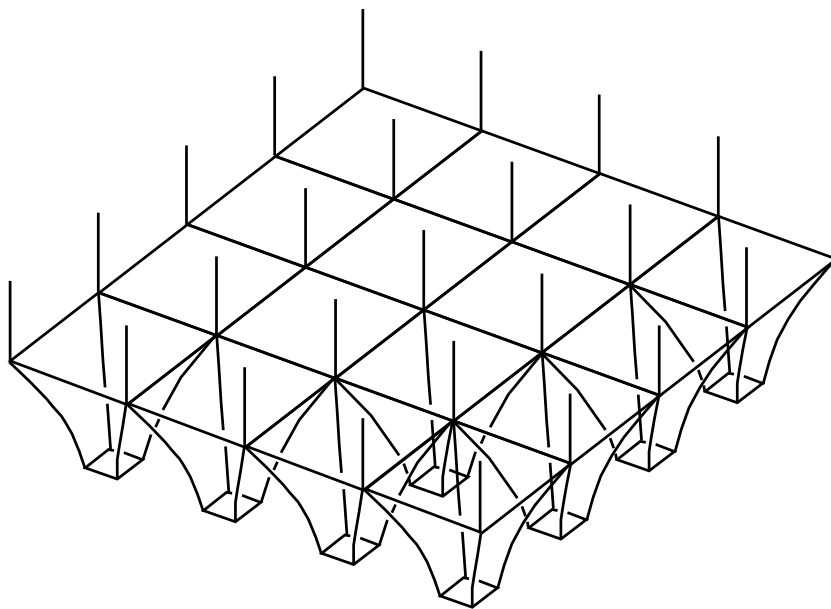
Figure 1. Array of 4×4 flux tubes merging into a space-filling field at the positive polarity end of a coronal loop. For clarity only 8 of the 16 flux tubes are drawn.

shows the flux tubes at the positive polarity end of the loop, and a similar array of flux tubes is present at the other end. The small squares indicate the cross-sections of the flux tubes at the base of the photosphere, and the large squares indicate the boundaries between flux tubes at the "merging height" where neighboring flux tubes come together. Just above the merging height the magnetic field is approximately uniform, as indicated by the vertical lines.

In plage regions the photospheric flux tubes are densely packed, but spatially separated from each other. In our model we assume that the medium between the flux tubes is field-free. Let $\overline{B_z}$ be the average magnetic flux density in the photosphere, i.e., the vertical component of magnetic field averaged over the flux tubes and the surrounding field-free medium. The magnetic field emerges from the Sun at one end of the coronal loop, where $\overline{B_z} > 0$, and reenters the Sun at the other end, where $\overline{B_z} < 0$. In this paper we construct a loop model in which the magnetic field strength varies along the loop, and the average field strength in the corona is 60 G (see next subsection). In this model the average magnetic flux density at the base of the photosphere is $|\overline{B_z}| = 181.6$ G, which is typical for the magnetic flux densities found in plage regions (e.g., Buehler et al. 2015). The flux density at the merging height is slightly lower because of the overall expansion of the loop.

Each flux tube has a magnetic field strength $B_0(z)$ that decreases with height z in the photosphere. The height $z = 0$ is defined as the *average* height of the surface where the optical depth $\tau = 1$ at wavelength $\lambda = 5000$ Å in the continuum. Buehler et al. (2015) observed magnetic flux concentrations in a plage region, and found field strengths of about 1520 G at optical depth $\log(\tau) = -0.9$. In kilogauss flux elements the surfaces of constant τ are depressed relative to the surrounding photosphere (Wilson depression). Therefore, in the present model we assume a field strength $B_0(0) = 1500$ G at the base of the photosphere ($z = 0$). The magnetic filling factor at height z is approximately given

by $f(z) \approx |\overline{B_z}|/B_0(z)$; in the present model $f(0) = 0.12$ at the base of the photosphere. The filling factor increases with height, and reaches unity at the so-called merging height ($z = z_m$), which lies in the upper photosphere or low chromosphere (e.g., Bruls & Solanki 1995). Above this height the different flux tubes come together to fill the available volume. Such merging of flux tubes into a space-filling field occurs at both ends of the coronal loop. Therefore, in our model the merged field extends from the chromosphere at one end of the loop to the chromosphere at the other end.

The flux tubes expand with height because of the stratification of the photosphere. To describe this expansion, we use the thin-tube approximation (Spruit 1976; Defouw 1976). The flux tubes are assumed to be in pressure balance with their surroundings:

$$\frac{B_0^2}{8\pi} = p_{\text{ext}}(z) - p_{\text{int}}(z), \tag{1}$$

where $p_{\text{int}}(z)$ is the internal gas pressure, and $p_{\text{ext}}(z)$ is the pressure in the field-free external medium. The atmospheres outside and inside the flux tubes are assumed to be in hydrostatic equilibrium:

$$p_{\text{ext}}(z) = p_{\text{ext},0} \exp\left[-\int_0^z \frac{dz'}{H_p(z')}\right], \tag{2}$$

$$p_{\text{int}}(z) = p_{\text{int},0} \exp\left[-\int_0^z \frac{dz'}{H_p(z')}\right], \tag{3}$$

where $H_p(z)$ is the pressure scale height in the photosphere, and $p_{\text{ext},0}$ and $p_{\text{int},0}$ are the external and internal gas pressures at the base of the photosphere (the "external" medium is present only below the merging height). Here we neglect temperature differences between the flux tubes and the external medium. At the base of the photosphere the external pressure $p_{\text{ext},0} = 1.274 \times 10^5$ dyne cm^{-2} (Spruit 1977), and the internal pressure $p_{\text{int},0} = 0.379 \times 10^5$ dyne cm^{-2}. We use simple analytic models for the temperature and mean molecular weight as functions of height in the solar atmosphere, which allows us to compute the pressure scale height $H_p(z)$ and magnetic field strength $B_0(z)$.

We then determine the merging height z_m as the point where $B_0(z)$ equals the field strength $B(s)$ from the global loop model described in the next subsection. We find that the merging height is located at $z_m \approx 520$ km in the temperature minimum region between the photosphere and chromosphere. At the merging height $B_0(z_m) \approx 176.6$ G, slightly lower than the flux density $\overline{B_z}$ at the base of the photosphere because of the overall expansion of the loop with height. We assume that at the base of the photosphere the flux tubes have widths $w_0 = 400$ km, which is consistent with the observed sizes of magnetic flux concentrations in plage regions (e.g., Buehler et al. 2015). The magnetic flux of each tube is $\Phi = w_0^2 B_0(0) = 2.4 \times 10^{18}$ Mx. The width $w_t(z)$ of each flux tube increases with height to conserve magnetic flux, $w_t(z) = w_0 \sqrt{B_0(0)/B_0(z)}$. At the merging height $w_t(z_m) = 1{,}165$ km, consistent with the typical distances between flux concentrations in plage regions (e.g., Buehler et al. 2015). In our model 4×4 flux tubes come together at the merging height, so the width of the merged field is $w_m(z_m) = 4w_t(z_m) \approx 4{,}660$ km.

The merged field contains many separatrix surfaces corresponding to the boundaries between flux tubes at the merging height (the large squares in Figure 1). In our model these are true separatrix surfaces, not quasi-separatrix layers, because in the photosphere the flux tubes are separated by field-free regions, so they are topologically distinct. There are two sets of separatrix surfaces, one from each end of the coronal loop. We assume that the flux-tube structures at the two ends are shifted relative

to each other by half the width of a flux tube, $w_t(z_m)/2$, in both the x and y directions. Hence, the separatrix surfaces from one end of the loop are located inside the flux tubes at the other end, and each flux tube is split into 4 distinct flux systems. Therefore, the magnetic structure considered here contains 64 different flux systems (four times the number of flux tubes). In the presence of transverse waves, electric currents can develop at the boundaries between these flux systems.

3.2. Large-Scale Structure of the Merged Field

On a larger scale the magnetic field extends from the photosphere at one end of the loop to the photosphere at the other end. Let s be the coordinate along the loop with $s = 0$ at the base of the photosphere at the positive polarity end of the loop, and $s = L$ at the other end. From now on the field strength $B_0(s)$, width $w_t(s)$ of a flux tube, and width $w_m(s)$ of the merged field will be written as functions of s, not height in the photosphere. The points where the flux tubes merge are located at $s_1 = z_m$ and $s_2 = L - z_m$, so the merged field extends from s_1 to s_2. This includes the coronal part of the loop, as well as the chromospheres and TRs at the two ends. The merged field is approximated as the potential field of a dipole located at some depth z_0 below the photosphere. We use a cartesian coordinate system (x', y', z) with the origin at the center of the bipolar region and z the height above the photosphere. The dipole is located at $x' = y' = 0$, $z = -z_0$, and is pointed in the $-x'$ direction. We also use a spherical coordinate system (r, θ, ϕ) centered at the dipole, where r is the radial distance from the dipole, θ is the angle relative to the $+x'$ axis, and ϕ is the azimuth angle ($\phi = 0$ corresponds to $y' = 0$ in the cartesian frame). Then the magnetic field is given by

$$B_r = -\mu \frac{2\cos\theta}{r^3}, \qquad B_\theta = -\mu \frac{\sin\theta}{r^3}, \tag{4}$$

where θ is the angle relative to the $+x'$ direction, and μ is the dipole strength ($\mu > 0$). The field lines lie in planes $\phi = $ constant, and their shapes are given by $r(\theta) = r_0 \sin^2\theta$, where r_0 is constant along a field line. For field lines in the plane $y' = 0$ we obtain the following cartesian coordinates

$$x'(\theta) = r_0 \sin^2\theta \cos\theta, \tag{5}$$
$$z(\theta) = r_0 \sin^3\theta - z_0. \tag{6}$$

We now consider the particular field line that intersects the photosphere at right angles, which implies $dx'/d\theta = 0$ at the two intersection points. Let $\theta(s)$ be the angle as function of position along this particular field line. Then equation (5) yields $\theta(0) = \pi - \theta_0$ and $\theta(L) = \theta_0$, where $\theta_0 \equiv \arccos(1/\sqrt{3})$, and equation (6) yield $r_0 = (3/2)^{3/2} z_0$. The intersection points are located at $x' = \mp x_0$, where $x_0 = z_0/\sqrt{2}$. We assume $x_0 = 30$ Mm, which implies $z_0 = 42.43$ Mm and $r_0 = 77.95$ Mm. The length of the loop between intersection points is obtained by numerical integration: $L = 103.3$ Mm. In this paper we consider a thin coronal loop surrounding the selected field line. The magnetic field strength along this loop is given by

$$B(s) = |\mathbf{B}| = \frac{\mu}{r_0^3} \frac{\sqrt{3\cos^2\theta(s) + 1}}{\sin^6\theta(s)}, \qquad \text{where} \quad \theta_0 \leq \theta(s) < \pi - \theta_0. \tag{7}$$

The dipole strength μ is chosen such that the average field strength along the loop is 60 G. Then the field strength at the base of the photosphere is $B(0) = B(L) = 181.6$ G. The field strength at the loop top is about 38 G. From the photosphere to the loop top the cross-section of the loop expands by a factor $\Gamma = (3/2)^3 \sqrt{2} = 4.77$.

3.3. *Wave Dynamics*

We simulate the dynamics of transverse waves inside the flux tubes (photosphere) and in the merged field (chromosphere and corona). The two regions are coupled such that waves can propagate from the flux tubes into the merged field and back. In the following we describe (a) the waves inside the flux tubes, (b) the waves in the merged field, and (c) the reduced MHD equations describing these waves. The coupling between the flux tubes and the merged field is described in the next subsection.

In this section we only consider the motions of plasma inside the photospheric flux tubes, not the transverse motions of the tubes themselves. The side boundaries of the flux tubes are assumed to have fixed positions. Therefore, we only simulate the Alfvén waves inside the flux tubes, not the kink waves that distort the shapes of the tubes. The flux tubes have square cross-sections. For each flux tube we introduce coordinates (x, y) in the planes perpendicular to the tube axis; these coordinates are in the range $-w_t/2 \leq x \leq +w_t/2$ and $-w_t/2 \leq y \leq +w_t/2$, where $w_t(s)$ increases with height above the photosphere. The velocity inside the flux tubes is assumed to be perpendicular to the flux tube axis, $\mathbf{v}(x, y, s, t) = v_x \hat{\mathbf{x}} + v_y \hat{\mathbf{y}}$, where $\hat{\mathbf{x}}$ and $\hat{\mathbf{y}}$ are unit vectors in the horizontal direction. The velocity is assumed to be nearly incompressible, $\nabla_\perp \cdot \mathbf{v} = 0$, and vanishes at the side boundaries of the tube: $v_x = 0$ at $x = \pm w_t(s)/2$, and $v_y = 0$ at $y = \pm w_t(s)/2$. At the base of the photosphere the velocities $\mathbf{v}(x, y, 0, t)$ or $\mathbf{v}(x, y, L, t)$ are imposed as boundary conditions (separately for each flux tube). These so-called "footpoint" motions vary randomly with time (see section 3.5), and are statistically independent for different flux tubes. The footpoint motions produce Alfvén waves that travel upward along the tubes. When the waves reach the merging height they propagate into the merged field above.

At the merging height 4×4 flux tubes with square cross-sections come together to form the merged field (see Figure 1). Therefore, the merged field also has a square cross-section, and the width $w_m(s)$ of the cross-section varies with position along the loop. At the merging heights $w_m(s_1) = w_m(s_2) = 4{,}660$ km. We introduce coordinates (x, y) perpendicular to the loop axis; these coordinates are in the range $0 \leq x \leq w_m(s)$ and $0 \leq y \leq w_m(s)$. The velocity is given by $\mathbf{v}(x, y, s, t) = v_x \hat{\mathbf{x}} + v_y \hat{\mathbf{y}}$, where $\hat{\mathbf{x}}$ and $\hat{\mathbf{y}}$ are now perpendicular to the loop axis, which is curved (see previous subsection). The velocity is again assumed to be nearly incompressible, $\nabla_\perp \cdot \mathbf{v} = 0$. For the merged field we assume periodic boundary conditions, so $\mathbf{v}(x + w_m, y, s, t) = \mathbf{v}(x, y + w_m, s, t) = \mathbf{v}(x, y, s, t)$, and similar for the magnetic fluctuations. The waves injected at the merging heights can travel upward along the loop and dissipate their energy in the chromosphere and corona via AWT. The waves can also travel back down into the flux tubes, and generate turbulence there. Therefore, the merged-field region contains a complex wave field generated by waves from multiple flux tubes at each end of the coronal loop.

The boundaries between the flux tubes at the merging height can be traced upward into the merged field, forming separatrix surfaces. Away from the merging heights these boundaries are no longer fixed, and can move with the transverse displacements of waves. Therefore, within the merged field wave energy can be exchanged between neighboring flux tubes. The velocity field may not be continuous at these boundaries because the waves on either side originate in different photospheric flux tubes and are statistically independent. Therefore, thin current sheets may develop at the boundaries between the flux tubes in the merged field. The dissipation of these boundary currents may provide an extra source of heat (in addition to the heat provided by AWT in a single tube).

The transverse waves are simulated using the reduced MHD approximation (e.g., Strauss 1976, 1997). The magnetic field strength $B_0(s)$ and density $\rho(s)$ are assumed to be constant over the cross-section both for the flux tubes and for the merged field. The magnetic and velocity fluctuations are described as a superposition of Alfvén waves propagating parallel and anti-parallel to the background field. The waves can be written in terms of Elsasser variables,

$$\mathbf{z}_\pm(x, y, s, t) = \mathbf{v} \mp \frac{\mathbf{B}_1}{\sqrt{4\pi\rho}}, \tag{8}$$

where $\mathbf{v}(x, y, s, t)$ is the plasma velocity, $\mathbf{B}_1(x, y, s, t)$ is the magnetic fluctuation, and $\rho(s)$ is the mean plasma density (Elsasser 1950). The two different wave types interact nonlinearly: the $\mathbf{z}_+$ waves are distorted by the counter-propagating $\mathbf{z}_-$ waves, and vice versa, which leads to a turbulent cascade of wave energy to smaller spatial scales (Iroshnikov 1963; Kraichnan 1965; Shebalin et al. 1983). The Alfvén waves are described in terms of stream functions $f_\pm(x, y, s, t)$ for the Elsasser variables:

$$\mathbf{z}_\pm(x, y, s, t) = \nabla_\perp f_\pm \times \hat{\mathbf{s}}, \tag{9}$$

where $\hat{\mathbf{s}}(x, y, s)$ is the unit vector along the background field. Then the velocity stream function $f = (f_+ + f_-)/2$, and the magnetic flux function $h = (f_- - f_+)/(2v_\mathrm{A})$, where $v_\mathrm{A}(s) \equiv B_0/\sqrt{4\pi\rho}$ is the Alfvén speed. The reduced MHD equations (e.g., Strauss 1976; Schekochihin et al. 2009; Perez & Chandran 2013, papers I and IV) can be written in the following form:

$$\frac{\partial\omega_\pm}{\partial t} = \mp v_\mathrm{A}\frac{\partial\omega_\pm}{\partial s} + \frac{1}{2}\frac{dv_\mathrm{A}}{ds}(\omega_+ - \omega_-) + \mathcal{N}_\pm + \tilde{\nu}_\pm\nabla_\perp^2\omega_\pm, \tag{10}$$

where $\omega_\pm \equiv -\nabla_\perp^2 f_\pm$ are the vorticities of the waves, $\mathcal{N}_\pm$ are nonlinear terms, and $\tilde{\nu}_\pm$ are artificial viscosities. The nonlinear terms are given by

$$\mathcal{N}_\pm = -\tfrac{1}{2}[\omega_+, f_-] - \tfrac{1}{2}[\omega_-, f_+] \pm \nabla_\perp^2\left(\tfrac{1}{2}[f_+, f_-]\right) \tag{11}$$

where $[\cdots, \cdots]$ is the bracket operator:

$$[a, b] \equiv \frac{\partial a}{\partial x}\frac{\partial b}{\partial y} - \frac{\partial a}{\partial y}\frac{\partial b}{\partial x}, \tag{12}$$

where $a(x, y)$ and $b(x, y)$ are two arbitrary functions. The four terms on the right-hand side of equation (10) describe wave propagation, linear couplings resulting from gradients in Alfvén speed, nonlinear coupling between counter-propagating waves, and wave damping. The numerical methods for solving these equations are described in Appendix A. We use Fourier analysis to describe the dependence of the waves on the x and y coordinates, and finite-differences in the s direction along the loop. To properly resolve the structure of the TR, we use a high-resolution grid with variable grid spacing (the smallest cells have $\Delta s = 0.3$ km). Also, to follow the waves as they propagate through the TR, we use very small time steps locally within the TR ($\Delta t < 0.001$ s). Therefore, we no longer treat the TR as a discontinuity, as we did in our earlier work (papers I, II and III). This allows us to more accurately evaluate the heating rates within the TR.

3.4. *Wave Coupling between Flux Tubes and Merged Field*

Consider a wave f_+ traveling upward in one of the flux tubes just below the merging height at $s = s_1$. When this wave reaches the merging height it can readily enter into the merged-field region, because the wave travels from the relatively narrow flux tube into the much wider merged field. Hence, there is no reflection of the wave as it reaches the merging level. However, the same is not true for waves traveling downward towards s_1. When a downward propagating wave f_- reaches the merging height, its transmission or reflection depends on the perpendicular wavenumber $k_\perp$ of the wave. If the perpendicular length scale $\pi/k_\perp$ of the wave is small compared to the width $w_t(s_1)$ of the flux tubes, the wave can be readily transmitted, but if $\pi/k_\perp > w_t(s_1)$ the wave must be partially reflected because the velocity field of the wave cannot satisfy the side boundary conditions of the flux tubes.

The transmission and reflection of downward propagating waves at the merging height are determined as follows. We first compute the stream functions $f'_\pm(x, y, s_1, t)$ of the waves at the bottom of the merged field according to equation (A5) (the grid refinement level $N = 0$ at this height). Let (x_b, y_b) be the coordinates of the edges of the flux tubes, as indicated by the large squares in Figure 1. Also, let $f'_b \equiv f'_-(x_b, y_b, s_1, t)$ be the values of the stream function for the f_- wave at these edges. We then compute the harmonic function $f^*(x, y, t)$ that satisfies $\nabla^2_\perp f^* = 0$ inside the squares and $f^*(x_b, y_b, t) = f'_b$ at the edges of the squares. This harmonic function does not satisfy the side boundary conditions in the flux tubes, which require $f(x_b, y_b, t) = 0$. Therefore, we assume that $f^*(x, y, t)$ is the part of the downward wave that is reflected back up into the merged field (Longcope & van Ballegooijen 2002). The remainder of the wave function is given by

$$\delta f(x, y, t) \equiv f'_-(x, y, s_1, t) - f^*(x, y, t), \tag{13}$$

which satisfies $\delta f(x_b, y_b, t) = 0$ and can be transmitted into the flux tubes. The transmission is implemented by setting $f_-(x, y, s_1, t) = \delta f(x, y, t)$ at the top of the flux tubes just below the merging height. The reflection is implemented by subtracting $f^*(x, y, t)$ from both wave types at the bottom of the merged field:

$$f_\pm(x, y, s_1, t) = f'_\pm(x, y, s_1, t) - \tfrac{1}{2} f^*(x, y, t). \tag{14}$$

The corrected stream function at the bottom of the merged field satisfies

$$f(x_b, y_b, s_1, t) = [f_+(x_b, y_b, s_1, t) + f_-(x_b, y_b, s_1, t)]/2 = 0, \tag{15}$$

so the corrected velocity is parallel to the edges of the flux tubes, and is continuous across the merging height, as required. A similar reflection occurs for the f_+ waves at the other merging height, $s = s_2$.

3.5. *Photospheric Footpoint Motions*

In the present model the Alfvén waves are launched by imposing random footpoint motions at the base of the photospheric flux tubes ($z = 0$) at both ends of the coronal loop. Therefore, the velocity fields $\mathbf{v}(x, y, 0, t)$ or $\mathbf{v}(x, y, L, t)$ are imposed as a boundary conditions within the flux tubes. For each flux tube the velocity stream function at the base is a sum of three modes:

$$f(x, y, t) = f_1(t) F_{1,1}(\tilde{x}, \tilde{y}) + f_2(t) F_{2,1}(\tilde{x}, \tilde{y}) + f_3(t) F_{1,2}(\tilde{x}, \tilde{y}), \tag{16}$$

where $\tilde{x} = x/w_0 + 0.5$ and $\tilde{y} = y/w_0 + 0.5$ are dimensionless perpendicular coordinates, and $F_{n_x, n_y}(\tilde{x}, \tilde{y})$ is the eigenfunction defined in equation (A2). The three modes have $(n_x, n_y) = (1,1)$, $(2,1)$ and

(1,2), respectively, so the first mode describes a rotational motion with a single cell, and the other modes each have two counter-rotating cells. The mode amplitudes $f_k(t)$ are random functions of time. The different driver modes within a flux tube are uncorrelated, and modes from different flux tubes are uncorrelated. The random functions are obtained by Fourier filtering a random number sequence, using the filter function $\exp[-(\tau_0 \nu)^2]$, where ν is the temporal frequency (in Hz) and τ_0 is a specified parameter. In this paper we use $\tau_0 = 180$ s, which corresponds to a correlation time $\tau_c = \tau_0/\sqrt{2\pi} \approx 72$ s. The filtered sequences are normalized such that each driver mode has an equal contribution to the root-mean-square of the velocity. We assume $v_{\mathrm{rms}} = 1.5$ km s^{-1}, similar to the value used in our earlier work (papers I, II and III).

3.6. *Construction of the Background Atmosphere*

In the Reduced MHD model the structure of the background atmosphere must be specified before the waves can be simulated. In the lower atmosphere the temperature $T(s)$ and mean molecular weight $\mu(s)$ are described using simple analytic models with a chromospheric temperature of 8000 K. The gas pressure $p(s)$ and density $\rho(s)$ in the lower atmosphere are computed from the hydrostatic equilibrium equation. In the chromosphere the pressure scale height $H_p(s)$ is increased by 20% to account for wave pressure forces.

The temperature $T(s)$ and density $\rho(s)$ in the transition region and corona are determined by solving the equations describing the energy balance of the coronal plasma (for details, see Appendix B). The energy equations (B14) and (B15) include the effects of wave heating, thermal conduction, enthalpy flux and radiative losses. The methods for solving these equations are similar to those used in Schrijver & van Ballegooijen (2005), except that in the present case the coronal pressure p_{cor} is treated as a free parameter of the model, and the heating rate $Q_{\mathrm{A}}(s)$ is a derived quantity. For the purpose of constructing the background atmosphere, we assume the Alfvén wave heating rate is of the form

$$Q_{\mathrm{A}}(s) = c_0 [B_0(s)]^n, \tag{17}$$

where c_0 is a constant and the power law exponent $n \geq 0$. The constant c_0 is determined from p_{cor} as part of the iteration process (see Appendix B). The radiative loss function $\Lambda(T)$ is taken from CHIANTI version 8 (Dere et al. 1997; DelZanna et al. 2015a), assuming coronal abundances (Schmelz et al. 2012). The loop modeling yields $T(s)$ and $\rho(s)$ as functions of position along the loop, as well as the heating rate $Q_{\mathrm{A}}(s)$ needed to maintain the assumed coronal pressure. The parameter p_{cor} also determines the height z_{TR} of the base of the transition region.

4. RESULTS FOR ALFVÉN WAVE TURBULENCE MODEL

In this section we describe results from 3D MHD simulations of Alfvén waves for the multi-flux-tube model presented in section 3. The background atmosphere for this model is constructed as follows. Using an estimated value for the coronal pressure p_{cor}, we set up the background atmosphere as described in section 3.6 and then simulate the wave dynamics as described in section 3.3. The waves are simulated for a period $t_{\mathrm{max}} = 3000$ s, which is sufficient to reach a statistically stationary state where turbulence is present everywhere along the loop. From these simulation results we derive the wave heating rate $Q_{\mathrm{tot}}(s)$, which is an average over the loop cross-section and over time. In the corona $Q_{\mathrm{tot}}(s)$ is not necessarily equal to the rate $Q_{\mathrm{A}}(s)$ assumed in the setup of the background atmosphere. We then adjust p_{cor} and the exponent n in equation (17) until an approximate agreement between

the two heating rates is obtained. The final condition $Q_{\text{tot}} \approx Q_A$ indicates that the loop is in thermal equilibrium such that the simulated wave heating is balanced by the radiative and conductive losses of the coronal plasma. We find that the thermal equilibrium condition is satisfied when $n \approx 1$ and $p_{\text{cor}} \approx 1.8$ dyne cm^{-2}. Note that this value of coronal pressure applies only for the particular set of model parameters described in section 3. For example, we assumed that the photospheric magnetic flux density $\overline{B_z} = 181.6$ G, the photospheric footpoint velocity $v_{\text{rms}} = 1.5$ km s^{-1}, and the coronal loop length $L_c = 98.4$ Mm. In the following we show results for (1) the properties of the background atmosphere, (2) the time-averaged wave properties, (3) the magnetic- and velocity structure of the waves, (4) the spatial and temporal variations of the heating, and (5) the effect of the waves on spectral line profiles.

4.1. *Background Atmosphere*

The properties of the background atmosphere are shown in Figure 2. Here various quantities are plotted as function of position along the loop (merged field and flux tubes). Since the Alfvén speed varies strongly with position, it is convenient to use the wave travel time $t_0(s) \equiv \int_0^s ds'/v_A(s')$ as the independent variable. In terms of this coordinate the two merging heights are located at 41.4 s and 145.0 s, the two TRs are located at about 70 s and 117 s, the loop top is located at 93.2 s, and the total wave travel time along the loop is 187.1 s. Figure 2(a) shows the position s (full curve) and height z (dashed curve) as functions of t_0. Note that the total loop length is about 103.3 Mm, and the height of the loop top is 35.5 Mm. In Figure 2(b) the temperature T is plotted as function of t_0, which causes the lower atmosphere ($T < 10^4$ K) to be greatly expanded compared to the corona ($T > 10^6$ K). The temperature plateaus with $T = 8000$ K in the chromosphere are located at $50 < t_0 < 70$ s and $117 < t_0 < 137$ s. In the corona the peak temperature $T_{\text{max}} = 2.496$ MK, which is less than the values of $3 - 4$ MK found at the peaks of the observed DEM distributions (e.g., Winebarger et al. 2011; Warren et al. 2011, 2012). Figure 2(c) shows the plasma density ρ, which varies over 7 orders of magnitude.

The magnetic field strength B_0 along the loop is shown in Figure 2(d). Note that the horizontal scale of the plot is strongly distorted by the fact that we plot B_0 as function of wave travel time t_0, not distance s. Also note that B_0 is continuous at the merging height, and the minimum field strength of 38 G occurs at the loop top. Figure 2(e) shows the widths $w_t(s)$ of the individual flux tubes, and the width $w_m(s)$ of the merged field. Here we also plot the locations of merging heights (dashed vertical lines) and TRs (dotted lines). Finally, Figure 2(f) shows the Alfvén speed v_A. Note that v_A increases from about 15 km s^{-1} in the photosphere to about 4000 km s^{-1} in the low corona, then drops to 1500 km s^{-1} at the loop top. The rise of v_A in the chromosphere and TR causes strong wave reflection. The resulting counter-propagating waves interact nonlinearly and produce AWT in the lower atmosphere (paper I).

4.2. *Time-Averaged Wave Properties*

Figure 3 shows various wave-related quantities as function of position along the loop, averaged over time t in the simulation ($200 < t < 3000$ s). In the photosphere these quantities are also averaged over the cross-sections of all flux tubes combined, and in the chromosphere and corona they are averaged over the cross-section of the merged field. Figure 3(a) shows the total energy density of the waves, and the contributions from magnetic- and kinetic energy. Note that in the chromosphere the kinetic energy dominates, while in low corona ($t_0 = 75$ s and $t_0 = 110$ s) the magnetic energy is more
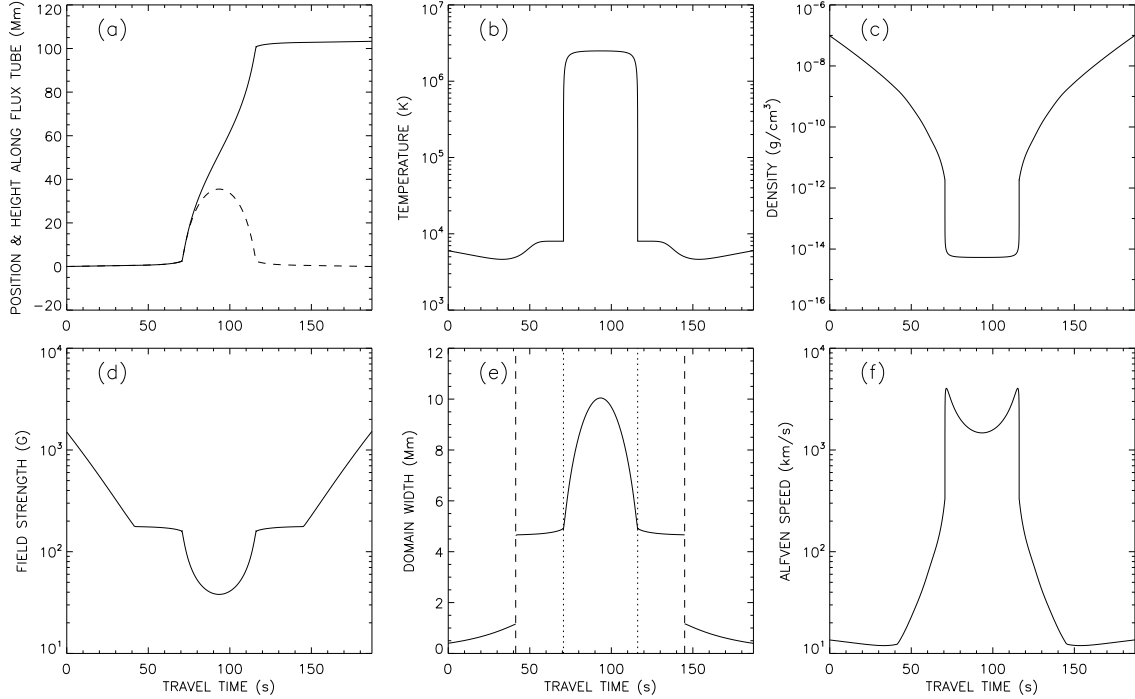
Figure 2. Parameters of the background atmosphere in a coronal loop. The parameters are plotted as function of the position along the loop, which is expressed in terms of the Alfvén travel time $t_0(s)$ from the positive-polarity footpoint. (a) Position s along the loop (full curve) and height z above the photosphere (dashed curve). (b) Temperature $T(s)$. (c) Mass density $\rho(s)$. (d) Magnetic field strength $B_0(s)$. (e) Width $w_t(s)$ of the individual flux tubes (for $t_0 < 41$ s, and $t_0 > 145$ s), and width $w_m(s)$ of the merged field (for $41 < t_0 < 145$ s). The dashed and dotted lines indicate the merging heights and TRs, respectively. (f) Alfvén speed $v_A(s)$.

important. Figure 3(b) shows the velocity amplitudes $v_{\rm rms}$ of the waves; this quantity peaks at the loop top, where $v_{\rm rms} \approx 30$ km s^{-1}. Figure 3(c) shows the vorticity, which peaks in the low corona. The maximum vorticity likely depends on the resolution of the numerical model.

Figure 3(d) shows the wave heating rate $Q_{\rm tot}(s)$ as predicted from the numerical simulations (black curve), as well as the contributions to $Q_{\rm tot}$ from waves propagating in the positive and negative s directions (red and green curves, respectively). Note that the heating rates in the corona are about 10^{-3} erg cm^{-3} s^{-1}, much smaller than those in the photosphere and chromosphere. We also plot the heating rate $Q_A(s)$ used in the setup of the background atmosphere (blue curve). Note that $Q_{\rm tot} \approx Q_A$, which is due to our choice for the coronal pressure, $p_{\rm cor} = 1.8$ dyne cm^{-2}. Looking at this figure more closely, we see that there are small jumps in $Q_{\rm tot}$ at the merging heights ($t_0 = 41.4$ s and $t_0 = 145.0$ s). These jumps indicate that the average heating rate in the region just above the merging height z_m is larger than that in the flux tubes just below z_m. As we will show later, this extra heating is due to electric currents at the interfaces between flux tubes in the chromosphere, where the tubes first come together. Figure 3(e) shows the amplitude $B_{1,\rm rms}$ of the magnetic field fluctuations. The largest fluctuations occur in the lower atmosphere. At the loop top $B_{1,\rm rms} \approx 1$ G, which is small compared to the local field strength, $B_0 = 38$ G. Figure 3(f) shows the rms value of the twist parameter, $\alpha \equiv (\nabla \times \mathbf{B})_\parallel / |\mathbf{B}|$. Note that in the coronal part of the loop the twist parameter is
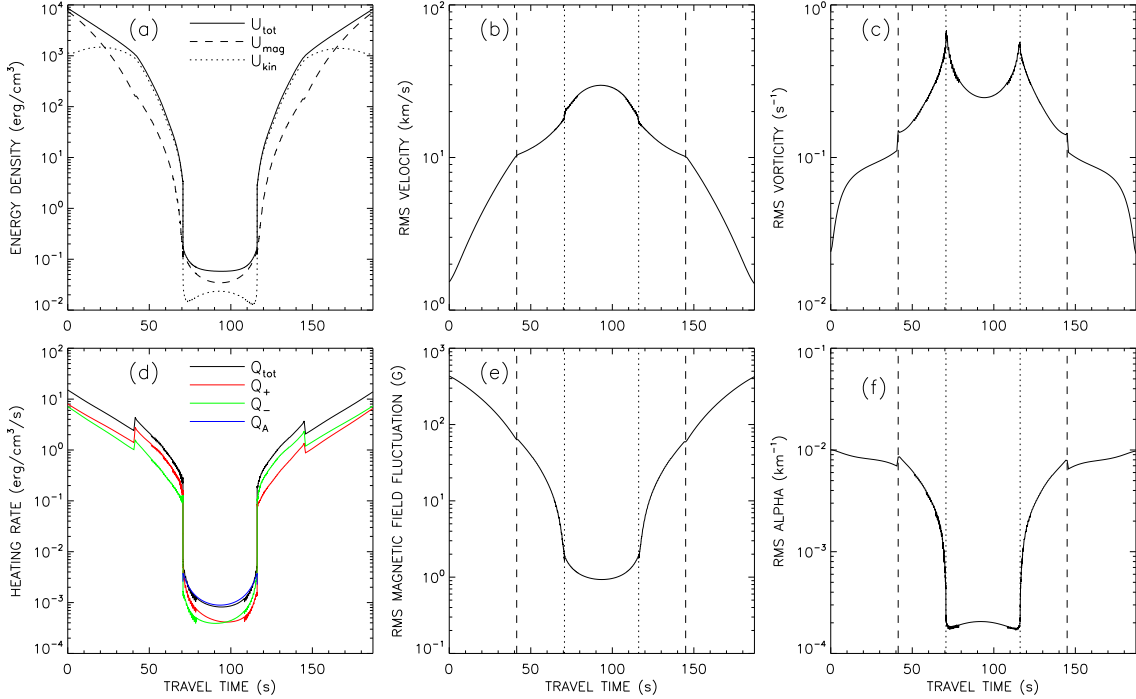
Figure 3. Model for Alfvén wave turbulence in a coronal loop. Various wave-related parameters are plotted as function of the position along the loop, which is expressed in terms of the Alfvén travel time $t_0(s)$ from the positive-polarity footpoint. (a) Kinetic and magnetic energy densities, and their sum $U(s)$. (b) Velocity amplitude $v_{rms}(s)$ of the waves. (c) Vorticity amplitude $\omega_{rms}(s)$. (d) Wave energy dissipation rates per unit volume: total wave dissipation rate $Q_{tot}(s)$ (black curve), rate Q_+ for waves traveling from left to right (red curve), rate Q_- for waves traveling from right to left (green curve), and plasma heating rate Q_A assumed in the setup of the background atmosphere (blue curve). (e) Amplitude of magnetic field fluctuations, $B_{1,rms}$. (f) Magnetic twist parameter, α_{rms}. In panels (b), (c), (e) and (f), the dashed and dotted lines indicate the merging heights and TRs, respectively.

more or less constant, $\alpha_{rms} \approx 2 \times 10^{-4}$ km^{-1}, indicating that the coronal field is close to a force-free state. However, in the lower atmosphere much larger values of α_{rms} are found, so the global magnetic field is far from a force-free state. This is a consequence of the fact that the photospheric footpoint motions produce wave-like disturbances with most of the inertia of the waves located in the lower atmosphere.

4.3. *Magnetic- and Velocity Structure of the Waves*

The magnetic structure of the loop is illustrated in Figure 4, where we plot the shapes of the magnetic field lines at the end of the simulation ($t = 3000$ s). The field lines are started from 48 randomly selected points in the cross-section at the loop top, and are traced downward along the legs of the loop and into the flux tubes at the two ends. The field-line tracing takes into account the overall curvature of the loop, the variation of the background field $\mathbf{B}_0(\mathbf{r})$, and the variation of the perturbations $\mathbf{B}_1(\mathbf{r})$. We use periodic boundary conditions at the side walls, so the field lines are not confined to the computational domain but may pass into neighboring regions. Figure 4(a) shows the field lines on the scale of the loop. Note that the field lines have small tilt angles relative to the loop axis, consistent with the fact that in our model $B_{1,rms} \ll B_0$ in the coronal part of the loop.
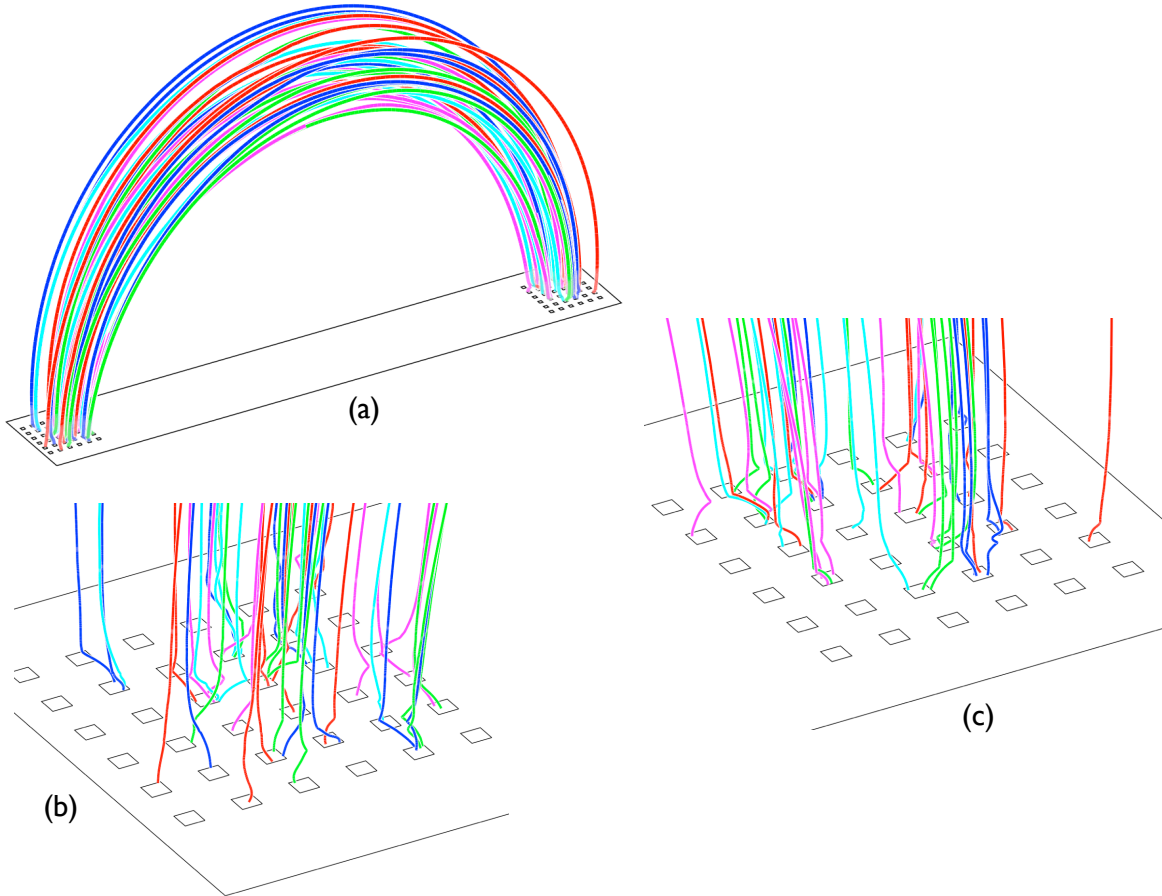
Figure 4. Magnetic field lines in a coronal loop heated by AWT. The colors of the field lines are randomly selected. (a) Large-scale view showing the coronal part of the loop. Note that the deviations from the (dipole) potential field are very small. (b) Close-up of the left footpoint, where the magnetic field breaks up into an array of discrete flux tubes. The squares indicate the intersections of the flux tubes with the plane $z = 0$. (c) Similar close-up of the right footpoint.

The tilt angles are only a few degrees, much smaller than the angles predicted for nanoflare models (e.g., Parker 1983; Pontin & Hornig 2015). However, such small angles appear to be consistent with the observed fine structures of coronal loops, which show only small deviations from the direction of the mean magnetic field (Schrijver et al. 1999; Antolin & Rouppe van der Voort 2012; Brooks et al. 2013; Scullion et al. 2014). Also, the fact that these angles are small is consistent with our use of the reduced MHD approximation. Figures 4(b) and 4(c) show close-ups of the two ends of the loop, where the field lines enter into the flux tubes (as sketched in Figure 1). The small squares indicate the intersections of the flux tubes with the base of the photosphere ($z = 0$). Note that there are small kinks in the field lines at the merging height. These kinks are due to the discontinuity of the horizontal components of the background magnetic field at the merging height.
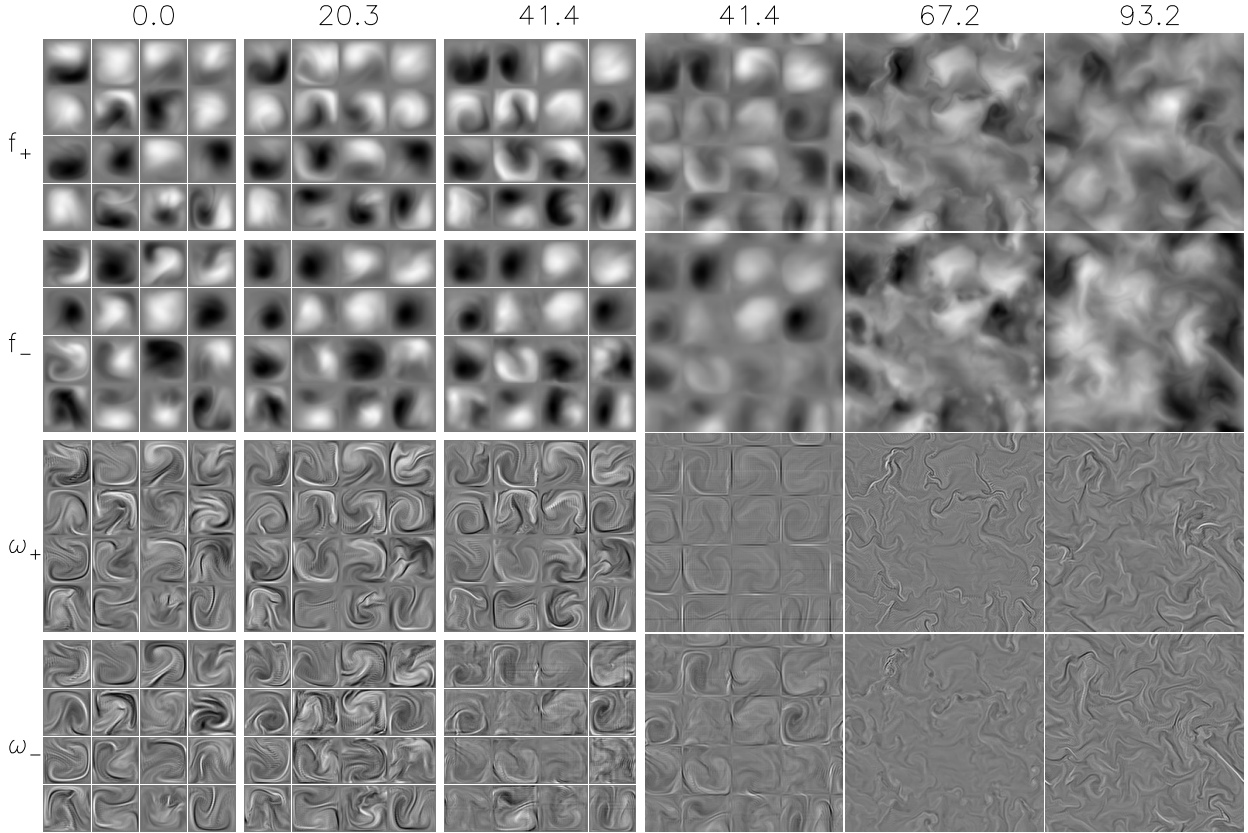
Figure 5. Spatial distribution of the Elsasser variables in a 3D MHD model for AWT in a coronal loop: velocity stream functions $f_\pm(x, y)$ (top rows) and vorticities $\omega_\pm(x, y)$ (bottom rows). The different columns correspond to cross-sections at different positions along the loop, and are labeled with the Alfvén travel time $t_0(s)$. The left three columns show cross-sections of the flux tubes in the photosphere at the positive polarity end of the loop, and the remaining columns show cross-sections of the merged field. The merging height is shown twice ($t_0 = 41.4$ s), and $t_0 = 93.2$ s corresponds to the loop top. The quantities $f_\pm$ and $\omega_\pm$ are shown as normalized greyscale images with white (black) indicating positive (negative) signals (see Figure 3 for information about the normalization and the actual width of each image).

Figure 5 shows the structure of the waves in cross-sections of the loop at time $t = 3000$ s. The diagram has four main rows: the first and second rows show the stream functions of the Elsasser variables, $f_\pm(x, y)$, and the third and fourth rows show the vorticities, $\omega_\pm(x, y)$, as functions of the perpendicular coordinates x and y. The figure also has six main columns, corresponding to different positions along the loop as indicated by the wave travel time t_0 at the top of each column. The first three columns show the waves in the flux tubes at the positive polarity end of the loop. In these columns f_+ is the upward propagating wave, and f_- is the downward propagating wave. For these three columns the wave patterns are shown as an array of 4×4 small images, each one corresponding to an individual flux tube (note that $f_\pm = 0$ at the side boundaries of the flux tubes). The size of these small images is normalized, and does not reflect the actual width $w_t(s)$ of the flux tubes. The last three columns show the wave patterns in the merged field in the left leg of the loop. Again, the size of these larger images does not reflect the actual width $w_m(s)$ of the merged field.

The merging height on the positive polarity side ($t_0 = 41.4$ s) is shown twice: in the third column as a collection of flux tubes, and in the fourth column as a merged field. Comparing the images for $f_+(x, y)$ in these two columns, we see that the waves in the flux tubes are nearly identical to those in the merged field. The reason is that a grid pattern is imposed on the upward propagating waves in the merged field, where $f_+ \approx 0$ at the grid boundaries. The stream function f_+ at these boundaries is not exactly zero because of wave reflection at the merging height (see section 3.4). A similar grid pattern can be seen for the downward propagating waves f_- at the merging height, which is due to wave reflection at larger heights in the chromosphere. This grid pattern is not visible in the upper chromosphere ($t_0 = 67.2$ s) and loop top ($t_0 = 93.2$ s), indicating that the boundaries between flux tubes have little effect on the waves at larger heights. The third and fourth rows of Figure 5 show the vorticities $\omega_\pm(x, y)$ of the Elsasser variables at the same positions along the loop. The actual vorticity is given by $\omega = (\omega_+ + \omega_-)/2$, and the current density is proportional to the twist parameter, $\alpha = (\omega_- - \omega_+)/(2v_A)$. Note that the vorticity is concentrated in thin layers where the magnetic field $\mathbf{B}_1$ and velocity field $\mathbf{v}$ change rapidly with position. Such current sheets and shear layers are naturally produced by the turbulent flow, and are further enhanced by discontinuities in the velocity at the boundaries between flux tubes at the merging height.

Note that the grid pattern in the merged field in the fourth column of Figure 5 is shifted relative to the pattern of the flux tubes in the third column. The shift is to the lower left, and its magnitude is one quarter of the width of a flux tube, or $w_t(z_m)/4$, in both the x and y directions. A similar shift occurs in the other leg of the loop (not shown), such that there is an overall shift of $w_t(z_m)/2$ between the flux tubes at the two ends. Therefore, the flux tubes at the two ends of the loop are not aligned with each other.

4.4. *Spatial and Temporal Variations of the Heating*

We now consider the plasma heating produced by the waves. In the present model the wave damping is described as ordinary diffusion, not hyper-diffusion as we did in our earlier work (papers I, II and III). The damping rates $\nu_{\pm,k}$ of the various wave modes are assumed to be proportional to the square of the perpendicular wavenumber (see Appendix A). This allows us to compute the spatial distribution of the wave dissipation rate $Q(x, y, s, t)$ as function of x and y. The wave energy dissipation rate is assumed to be equal to the heating rate of the plasma. Figure 6 shows the spatial distribution of the heating at two different times near the end of the simulation (top and middle rows), as well as its time average over the duration of the simulation (bottom row). The different columns correspond to different positions along the loop, as indicated by the labels at the top of each column. The heating rates are shown on a logarithmic scale, but a different scale is used for each column (see color bars at the top). Note that the instantaneous heating rates vary by more than 2 orders of magnitude over the cross section of the loop for all heights. Most of the heating occurs in current sheets and shear layers. At the merging heights the strongest heating occurs near the boundaries between flux tubes, which have fixed positions. However, in the TR and corona the location of the current sheets changes rapidly with time, so the spatial distribution of the heating also changes rapidly (compare upper and middle rows, which have a time difference of only 50 s). When the heating rates are averaged over time, the spatial variations across the loop become much less pronounced (see bottom row). At the merging height the time-averaged rate shows a strong grid pattern due to the underlying flux tubes, but the pattern is much weaker at the TRs, and absent at the loop top. Therefore, the effect of the
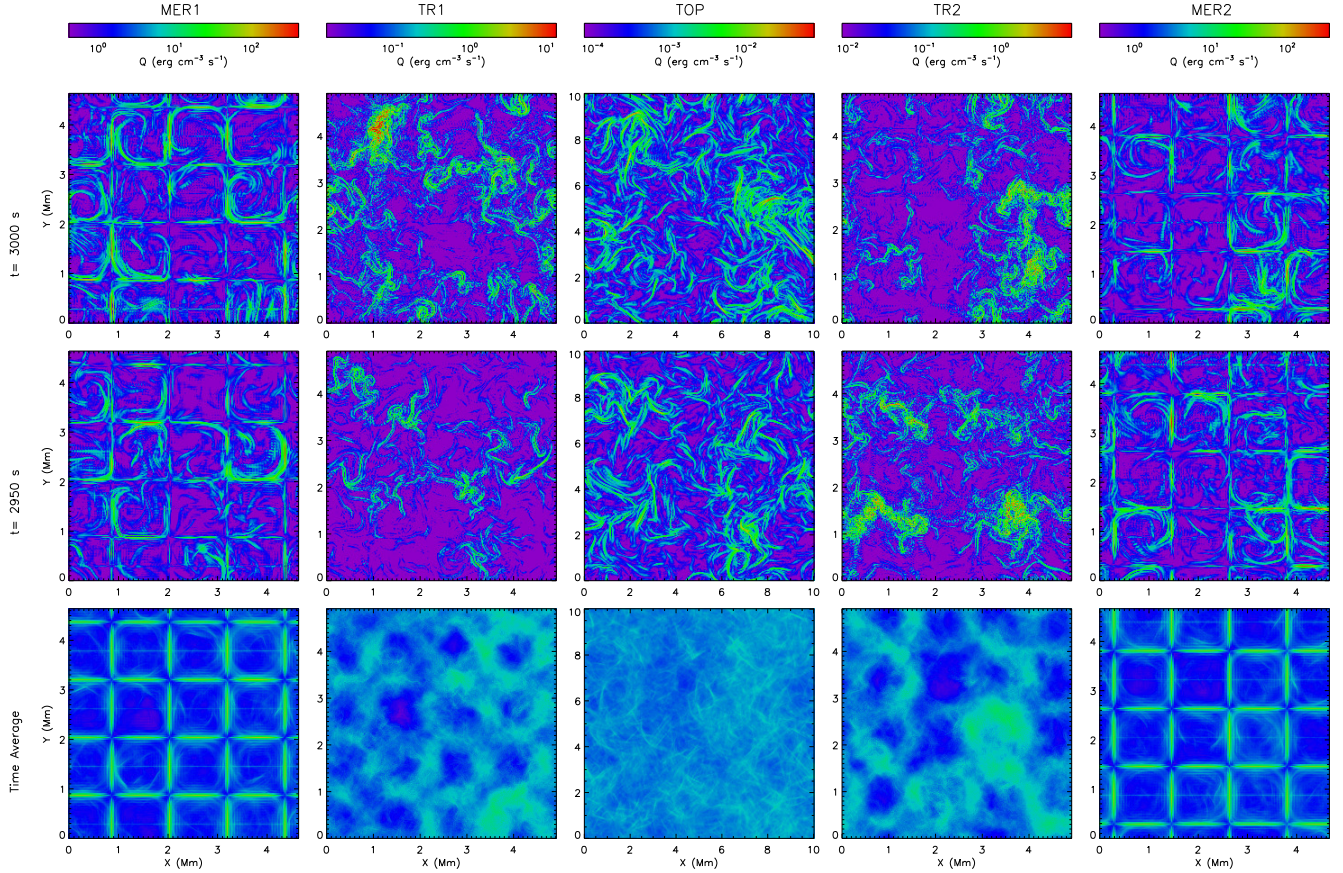
Figure 6. Spatial distribution of the heating rates in a 3D MHD model for AWT in a coronal loop. The top and middle rows show the heating at times $t = 3000$ s and $t = 2950$ s, respectively; the bottom row shows the heating rate averaged over the time interval $200 < t < 3000$ s. The different columns correspond to different positions along the loop, as indicated by the labels at the top of each column: MER1 and MER2 are the merging heights, TR1 and TR2 are the chromosphere-corona transition regions, and TOP is the loop top. Each image shows the rate $Q(x,y)$ as a function of the perpendicular coordinates x and y, and normalized as shown by the color bar at the top of each column. Note that the color scales are logarithmic.

flux tubes does not extend into the corona, and at the loop top the time-averaged heating rate is nearly uniform across the loop (see image in middle column, bottom row).

To understand how the plasma might respond to the heating, it is useful to determine how the heating rate $Q(t)$ varies with time t for a point moving with the flow. We randomly select various points in different cross-sections of the merged field, and track these points for the duration of the simulation. In the reduced MHD model the flows along the background field are neglected, so each point remains in the cross-section where it was originally located, but its perpendicular coordinates $x(t)$ and $y(t)$ vary with time. We measured the heating rates $Q(t)$ at such co-moving points. The results are shown in Figure 7 for four points at different positions along the loop. In all cases the heating is found to be very intermittent with strong heating events superposed on a background of much weaker heating. The magnitude of the heating events can be compared with the thermal energy density of the plasma, $E_{\rm th} = (3/2)p$, where p is the plasma pressure. Figure 7(a) shows the heating rate for a co-moving point at the merging height, $z_m = 518$ km. Note that there are about
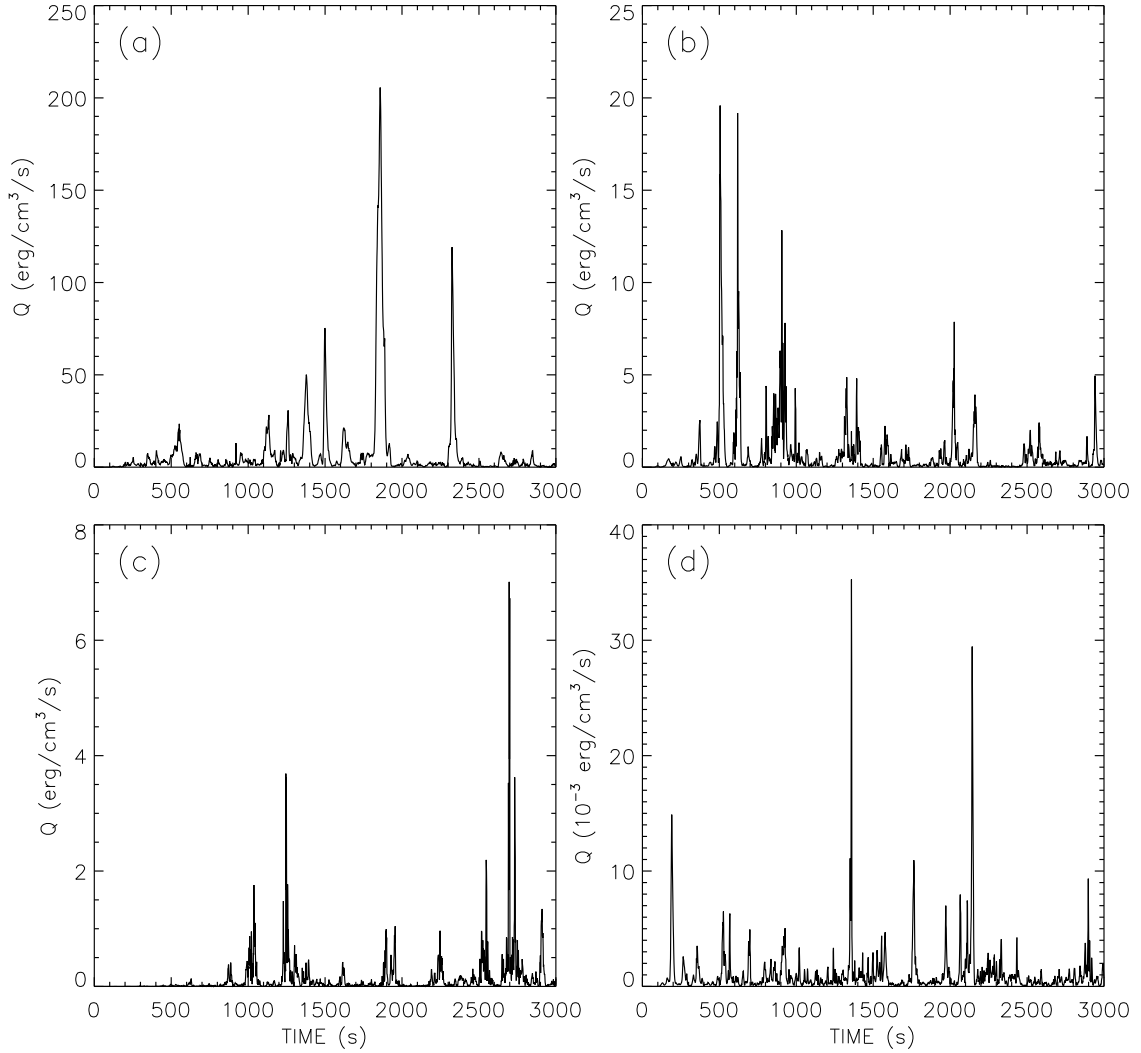
Figure 7. Heating rate $Q(t)$ as function of time for random points moving with the flow at different positions along the loop: (a) merging height; (b) mid-chromosphere, (c) transition region, (d) loop top.

8 events with peak heating rates in excess of 20 erg cm^{-3} s^{-1}. Each event lasts about 20 – 80 s and produces about 400 – 4000 erg cm^{-3}, comparable to the thermal energy density at that height, $E_{\rm th} \approx 823$ erg cm^{-3}. Therefore, such heating events are expected to produce significant increases in the local temperature. Figure 7(b)) shows the heating rate for a point in the middle chromosphere ($z = 1696$ km), where the heating events are an order of magnitude weaker. However, the thermal energy density is also much smaller, $E_{\rm th} \approx 15.8$ erg cm^{-3}, so again we expect significant temperature variations. The same is true for the base of the TR ($z = 2467$ km), where $E_{\rm th} \approx 2.7$ erg cm^{-3} (see Figure 7(c)). Finally, Figure 7(d) shows the heating rate for a co-moving point at the loop top. There are about 13 events with peak heating rates in excess of 0.004 erg cm^{-3} s^{-1} and durations of about 20 s, so each event produces about 0.08 erg cm^{-3}. This is small compared to the thermal energy density at the loop top, $E_{\rm th} \approx 2.7$ erg cm^{-3} s^{-1}, so the simulated heating events are not expected

to produce large temperature fluctuations at the loop top. This is consistent with earlier results in paper II, where we considered heating rates averaged over the loop cross-section.

The present AWT model predicts that the time-averaged heating rate $\overline{Q}(x, y, s)$ is enhanced at the boundaries between the flux tubes in the chromosphere, i.e., there is extra heating at the separatrix surfaces in the chromosphere. In the region just above the merging height, the time-averaged heating rate $Q_{\rm tot}(s)$ is enhanced by about a factor 2 compared to its value just below the merging height. However, this extra heating at the flux tube boundaries does not extend to large heights. At the height of the TR, the boundary heating is relatively weak, and at the loop top the time-averaged rate $\overline{Q}(x, y, s)$ is more or less constant over the cross-section of the loop. The reason for this rapid decline of the boundary heating with height is that the waves in the chromosphere are quite turbulent, and produce large displacements of the separatrix surfaces. Therefore, the extra energy associated with the discontinuities in the velocity at the merging height is quickly dissipated.

4.5. *Effect of the Waves on Spectral Line Profiles*

Spectroscopic observations of coronal loops show that the observed emission lines are significantly broadened in excess of their thermal widths (e.g., Doschek et al. 2007; Doschek 2012; Young et al. 2007; Tripathi et al. 2009; Warren et al. 2011; Tripathi et al. 2011; Tian et al. 2011, 2012a,b). Transverse MHD waves may contribute to this broadening, and at high spatial resolution it may be possible to directly observe the Doppler shifts associated with such waves. To compare the present model with observations, we simulate the effect of the modeled waves on the Doppler shift and Doppler width of an observed spectral line, assuming that the coronal loop is viewed from the side (in the $+y$ direction). Then the line-of-sight (LOS) velocity is given by v_y, and the observed Doppler shift is proportional to $< v_y >$, the mean value of v_y along the LOS. Also, the non-thermal component of the Doppler width is proportional to the velocity variance σ_y, which is given by $\sigma_y^2 = < v_y^2 > -(< v_y >)^2$. We assume for simplicity that the emissivity and thermal width of the spectral line are constant over the loop cross-section. Then $< v_y >$ and $< v_y^2 >$ can be approximated as simple averages over the y coordinate in our numerical model. To account for instrumental effects, we must also average in the x direction over a distance $\Delta x = D_0 \Delta \theta$, where $\Delta \theta$ is the angular resolution of the instrument and D_0 is the Sun-Earth distance.

Figure 8 shows the Doppler velocities at time $t = 1906$ s in the simulation. The three columns show maps of emission intensity (INT), average line-of-sight velocity (VLOS), and average non-thermal velocity (VNTH). The top row shows such maps for the full resolution of our numerical code, and the other rows give maps where spatial smearing and pixelation have been applied to the data. The middle row represents a hypothetical future instrument with a spatial resolution element size of 290 km (FWHM) and pixel size of 121 km, when projected onto the Sun. The bottom row is for the EIS instrument on *Hinode*, which has a spatial resolution element of about 1450 km (2") and pixel size of 725 km (1"). In these images only the merged magnetic field is shown, and the loop curvature is neglected, so each image is the projection of the loop on the (s, x) plane. Note that the width $w_m(s)$ of the merged field varies with position s along the loop. The vertical size of each image corresponds to a width of 10 Mm, and the vertical scale is expanded compared to the horizontal scale to show more clearly the velocity structures inside the loop. The left column shows the intensity using an inverted grey-scale (black is bright). At full resolution the edges of the observed structure are sharp because the loop is assumed to have a square cross-section (see section 3) and the emissivity is
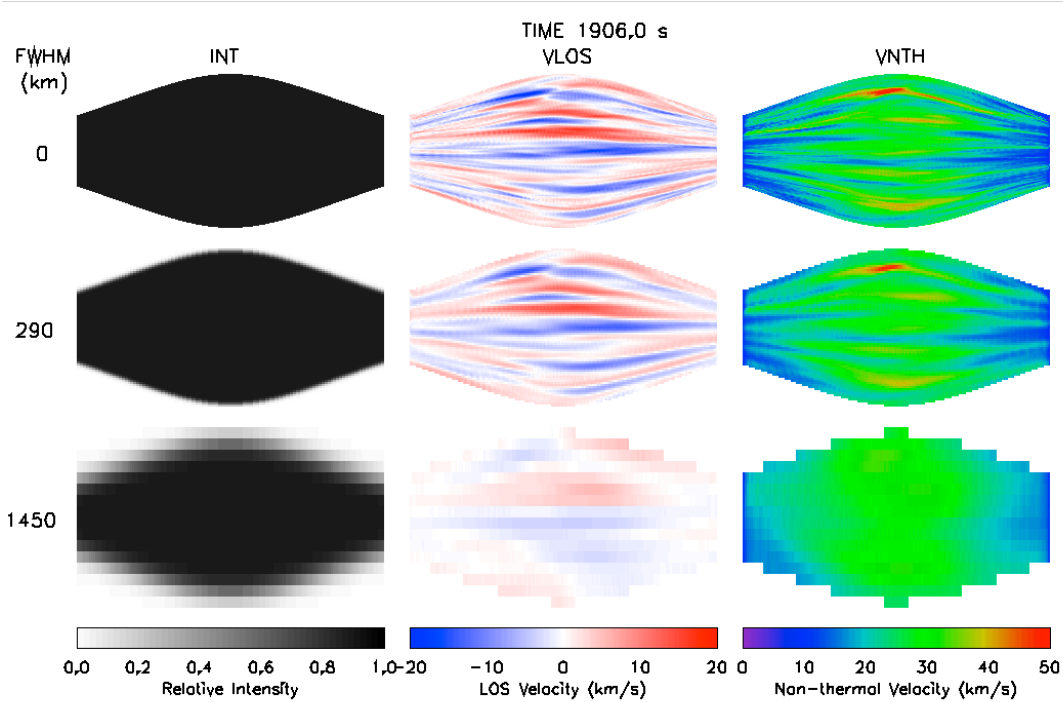
Figure 8. Effect of the modeled waves on the Doppler shift and Doppler width of a spectral line, assuming the loop is viewed from the side. The three column show the intensity (INT), line-of-sight velocity (VLOS), and non-thermal velocity (VNTH). The three rows correspond to different values of the spatial resolution of the instrument ($\Delta x = 0$, 290 and 1450 km). Each image shows a side view of the loop. The loop curvature is neglected, so the loop axis runs horizontally through the middle of each image. The transverse (vertical) scale is greatly expanded compared to the longitudinal scale. The velocity amplitudes are indicated by the color bars.

assumed to vanish outside the simulation domain. At lower resolution the edges become more fuzzy and the pixel size becomes more obvious.

The middle column of Figure 8 shows the predicted VLOS as a color-scale image. The velocity scale is given at the bottom of the column. The upper panel shows the velocity map at full resolution. Note that VLOS changes rapidly in the x direction (vertical) but gradually in the s direction (horizontal), indicating the internal motions are coherent along the loop. At the loop top (middle of image) the perpendicular variations occur on a length scale of about 500 km. The rms value of VLOS over the entire image is 5.8 km s^{-1}. The middle panel shows VLOS as observed with an instrument that has a spatial resolution of 290 km. The pattern is basically unchanged (rms velocity 5.1 km s^{-1}), indicating that the velocity variations would be well resolved in such observations. The bottom panel shows the velocity pattern expected for EIS observations. In this case the velocity amplitude is only 2.7 km s^{-1}, which is below the sensitivity of the EIS instrument. Therefore, EIS is not expected to

be able to observe the VLOS fluctuations simulated here, and indeed, EIS observations do not show clear evidence for such fluctuations.

The right column of Figure 8 shows the predicted non-thermal velocity (VNTH), and the corresponding velocity scale is given at the bottom of this column. The value of VNTH averaged over the image is about 27 km s^{-1}, nearly independent of resolution. This is somewhat higher than the non-thermal velocity of 17.6 ± 5.3 km s^{-1} measured with EIS (Brooks & Warren 2016), the most-probable velocity of 15 km s^{-1} observed with IRIS (Testa et al. 2016), and the values of $14 - 26$ km s^{-1} observed at the Norikura Solar Observatory (Hara & Ichimoto 1999). Therefore, the transverse waves in our model have relatively high velocities that are only marginally consistent with the available spectroscopic observations.

4.6. *Summary*

We have seen that the simulated AWT can produce only enough heat to maintain the coronal loop at a pressure $p_{\mathrm{cor}} = 1.8$ dyne cm^{-2} and peak temperature $T_{\mathrm{max}} = 2.5$ MK. The heating rate Q varies strongly in space and time, but the time-averaged heating rate in the corona is nearly constant across the loop, and the temperature fluctuations are predicted to be relatively small (see section 4.4). In contrast, the observations show that active regions have broad temperature distributions (e.g., Winebarger et al. 2011; Warren et al. 2011, 2012) with peaks of the observed DEM distributions at temperatures of $3 - 4$ MK. Therefore, the value of T_{max} predicted by our model is not quite high enough, and the model cannot readily explain the observed broad temperature distributions of active regions. However, the transverse velocities in our model are already quite high (see section 4.5), so enhancing the heating rate by increasing the footpoint velocity would likely produce a disagreement with the spectroscopic observations. Therefore, it makes sense to consider an alternative model for coronal heating.

5. MAGNETIC BRAIDING MODEL

The model presented in sections 3 and 4 assumes that the flux tubes are located on a square lattice (see Figure 1), and the tubes do not move horizontally. This allowed us to focus on waves *inside* the flux tubes, which have periods less than about 1 minute and are significantly amplified as they propagate upward through the photosphere and chromosphere. We did not include the longer-term motions of the flux tubes themselves. However, observations show that photospheric flux elements exhibit random motions on a wide range of time scales (e.g., DeVore et al. 1985; Wang 1988; Schrijver & Martin 1990; Muller et al. 1994; Komm et al. 1995; Schrijver et al. 1996; Berger & Title 1996; Hagenaar et al. 1999; Utz et al. 2010; Abramenko et al. 2011; Wedemeyer-Böhm et al. 2012; Chitta et al. 2012). In the magnetic braiding model the coronal field lines are assumed to be braided by random footpoint motions on time scales of tens of minutes to hours, which must be motions of the flux tubes themselves. The observed random motions can be characterized in terms of a photospheric diffusion constant D, and in magnetic network and plage regions D is in the range $60 - 250$ km^2 s^{-1} for motions on time scales of tens of minutes to a few days (Berger et al. 1998). It is desirable to include the observed random motions also in our wave heating model. However, in reduced MHD the magnetic field strength B_0 must be constant across the modeled structures, so we must separately describe each flux tube, as well as the merged field, and the field-free regions between the flux tubes cannot be included in the model. When the flux tubes have variable positions in the (x, y) plane,
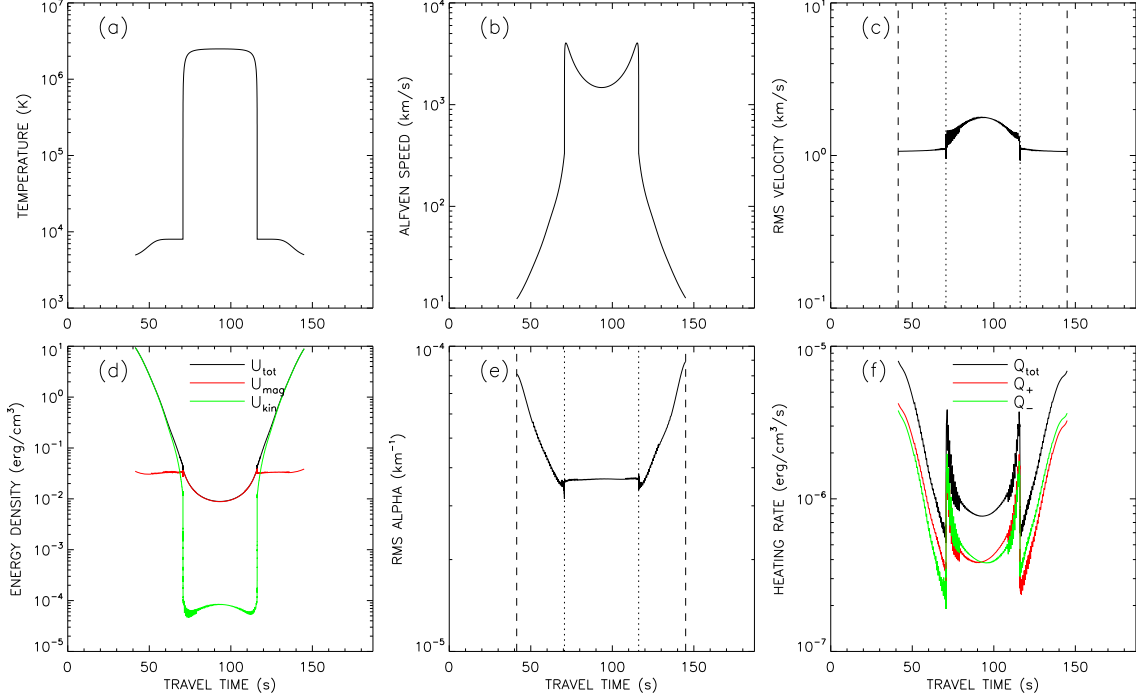
Figure 9. Various quantities as function of position along the loop for the magnetic braiding model: (a) temperature T, (b) Alfvén speed v_A, (c) velocity v_{rms}, (d) total energy density U_{tot} and contributions from magnetic- and kinetic energy, (e) magnetic twist parameter α_{rms}, (f) total energy dissipation rate Q_{tot} (black curve), and contributions $Q_\pm$ from the two different wave types (red and green curves). In panels (c) and (e), the dashed and dotted lines indicate the merging heights and TRs, respectively.

their cross-sections cannot be square, and their relationship to the merged field becomes too complex to describe in a reduced MHD model.

In this section we present a model in which the photospheric flux tubes have been removed, and the "footpoint" motions are applied directly at the merging heights ($z_m \approx 520$ km). For each end of the coronal loop the imposed velocity field has components $v_x(x, y, t)$ and $v_y(x, y, t)$, which describe the slow, random motions that would have been produced at the merging heights by the underlying flux tubes, if they had been included in the model. We find that such motions produce braiding of the coronal field lines, so we call this the magnetic braiding model. Note that a variety of "braiding models" are discussed in the literature, and different authors use different assumptions for the initial- and boundary conditions on the braided field. For example, in some models the magnetic field is approximated as a collection of discrete strands, so the field is not space-filling (e.g., Berger & Asgari-Targhi 2009; Berger et al. 2015). In other models the magnetic field is space-filling, but the photospheric field is concentrated in discrete flux elements that move about on the solar surface (e.g., Parker 1983; Berger 1991, 1993; Priest et al. 2002; Janse et al. 2010). It is found that thin current sheets develop at the interfaces between the flux tubes in the corona, and magnetic reconnection events ("nanoflares") are predicted to occur in these sheets (Parker 1988). These magnetic braiding models implicitly assume that the photospheric flux tubes have long lifetimes, and that the flux tubes can be wrapped around each other for many hours before reconnection is triggered (Parker 1983). In the present work we assume that the braided field is space-filling, but the photospheric flux tubes are

not included in the model. The velocities $v_x(x, y, t)$ and $v_y(x, y, t)$ at the merging height are assumed to be continuous functions of position, so there are no topologically distinct flux tubes in the corona. This assumption of spatial continuity of the footpoint motions is often used in numerical simulations of the build-up and evolution of braided magnetic fields (e.g., van Ballegooijen 1988; Mikić et al. 1989; Galsgaard & Nordlund 1996; Rappazzo et al. 2007, 2008, 2013; Dahlburg et al. 2016). Other authors focus on the turbulent relaxation of braided fields, and assume that the braided field is present in the initial state of the simulation (e.g., Wilmot-Smith 2015; Pontin & Hornig 2015; Pontin et al. 2017), so in these models the build-up of the braided field is not simulated. For the build-up of a braided field to occur, the onset of reconnection must be delayed as long as possible (Pontin & Hornig 2015). It is still an open question whether the observed random motions of photospheric magnetic elements can produce the kind of braided fields needed in nanoflares models.

In the present model we assume that $v_x(x, y, t)$ and $v_y(x, y, t)$ are continuous functions of position, so we neglect the spatial discontinuities in velocity that would naturally occur at the boundaries between neighboring flux tubes at the merging height. This has the effect of delaying the onset of reconnection as long as possible, and maximizes the build-up of energy in the braided field. Observations suggest that the motions of neighboring flux elements are uncorrelated. Therefore, we assume that the correlation length $L_\perp$ of the velocity field is equal to the width of a flux tube at the merging height, $L_\perp \approx 1{,}100$ km, and there are 28 driver modes. The rms velocity is $v_{\rm rms} = 1$ km s^{-1}, and the velocity auto-correlation time is $\tau_{\rm c} = \tau_0/\sqrt{2\pi} \approx 399$ s, where $\tau_0 = 1000$ s is the Fourier filtering parameter described in paper I. Using these values, we determine the random velocity field at each end of the loop. We then select 300 points randomly distributed over the simulation domain at the merging height, and follow these points for 6000 s as they move with the flow. The mean square displacement $< r^2(t) >$ of the particles increases more or less linearly with time, as expected for random walk. By fitting the results to the expression $< r^2(t) > = 4Dt$, we find $D \approx 200$ km^2 s^{-1}, which is at the high end of the range of observed diffusion constants (see Berger et al. 1998).

The structure of the background field in the magnetic braiding model is exactly the same as in the AWT model, and the methods for solving the reduced MHD equations are the same as in section 3.3 for the merged field. Since the flux tubes are omitted, we cannot simulate the short-period waves that emanate from these flux tubes. However, we assume that the heating produced by such short-period waves is still present. Therefore, we take $p_{\rm cor} = 1.8$ dyne cm^{-2}, the same as in the AWT model (section 4). Hence, the background atmosphere for the magnetic braiding model is the same as that shown for the merged field in Figure 2.

The dynamics of the braided field was simulated for a period of 8000 s. Figure 9 shows various quantities as function of position along the loop, expressed in terms of the wave travel time $t_0(s)$. As a reference, Figures 9(a) and 9(b) show the temperature $T(s)$ and Alfvén speed $v_A(s)$, which are the same as in Figure 2. The other panels show various quantities averaged over the loop cross-section and over time. Figure 9(c) shows the rms velocity of the waves. Note that the peak velocity in the corona is only about 1.8 km s^{-1}. Figure 9(d) shows the total energy density $U_{\rm tot}$ of the perturbations (black curve), the magnetic energy density $U_{\rm mag}$ (red curve), and the kinetic energy density $U_{\rm kin}$ (green curve). In the corona $U_{\rm mag} \gg U_{\rm kin}$, so the perturbations are dominated by the magnetic field, as expected for a magnetic braiding model. However, in the chromosphere the kinetic energy dominates, even though the rms velocity is only about 1.1 km s^{-1}. Figure 9(e) shows the rms value of the twist parameter, $\alpha \equiv (\nabla \times \mathbf{B})_\parallel / |\mathbf{B}|$. Note that $\alpha_{\rm rms}(s)$ is nearly constant in the coronal part
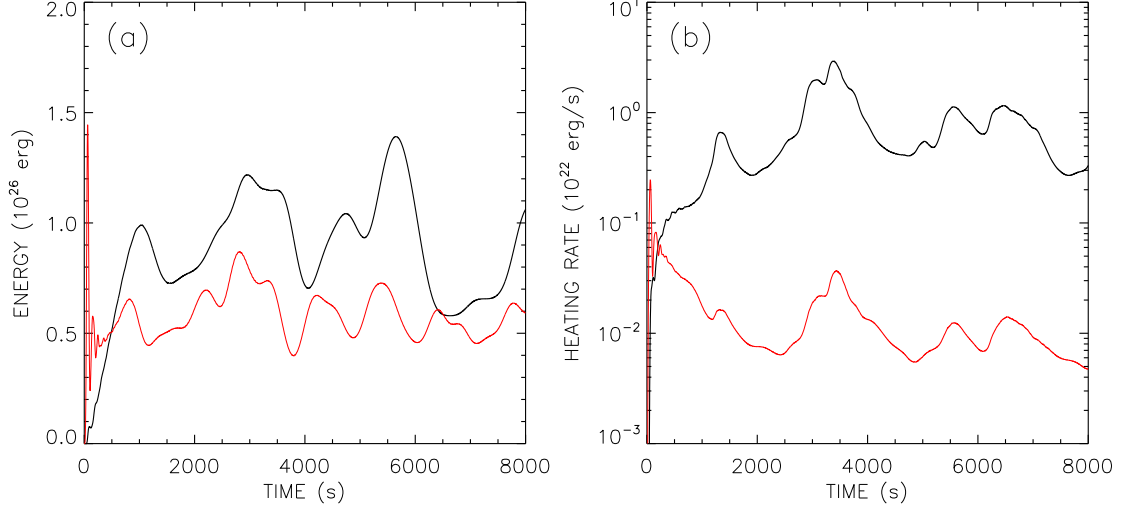
Figure 10. Free energies and heating rates as functions of time for the magnetic braiding model. (a) Total energy $W_{cor}(t)$ integrated over the coronal part of the loop (black curve), which is dominated by magnetic free energy of the braided field, and total energy $W_{chrom}(t)$ integrated over the chromospheric parts of the loop (red curve), which is dominated by kinetic energy. (b) Total heating rates integrated over the coronal and chromospheric parts of the loop (black and red curves, respectively).

of the loop, indicating that the magnetic field is close to a nonlinear force-free state, $\nabla \times \mathbf{B} \approx \alpha \mathbf{B}$, with α constant along the field lines. However, $\alpha_{rms}(s)$ is not constant in the chromospheres at either end of the loop, which is due to wave-like perturbations in the lower atmosphere.

Figure 9(f) shows the total energy dissipation rate $Q_{tot}(s)$ (black curve) for the magnetic braiding model, as well as the contributions $Q_\pm$ from perturbations propagating in opposite directions along the loop. Comparison with Figure 3(d) shows that these dissipation rates are much smaller than those in the AWT model. For example, in the corona $Q_{tot} \sim 10^{-6}$ erg cm^{-3} s^{-1}, whereas in the AWT model $Q_{tot} \sim 10^{-3}$ erg cm^{-3} s^{-1}. Therefore, the magnetic braids associated with the slow random motions of the flux tubes add an insignificant amount of heat compared to the energy provided by the short-period waves inside the flux tubes. By itself, the contribution from magnetic braiding is much smaller than the heating rate needed to maintain the background atmosphere with $T_{max} = 2.5$ MK and $p_{cor} = 1.8$ dyne cm^{-2}. The main reason for the low heating rates compared to the AWT model is that there is almost no amplification of the waves as they propagate upward through the chromosphere. The rms velocity in the corona is only about $1.1 - 1.8$ km s^{-1}, much smaller than the velocity in the AWT model. This lack of wave amplification is due to the long correlation time τ_c of the footpoint motions compared to the wave travel time in the chromosphere.

The total energy $W_{cor}(t)$ of the disturbances in the coronal part over the loop was computed by integrating the energy density $U_{tot}(s, t)$ over the coronal part of the volume, including the TRs at the two ends. Similarly, the energy $W_{chrom}(t)$ in the chromosphere was determined by integrating over the two chromospheric parts of the volume. Figure 10(a) shows $W_{cor}(t)$ (black curve) and $W_{chrom}(t)$ (red curve), plotted as functions of time t in the simulation. The coronal energy increases with time over the first 1000 seconds of the simulation, but then reaches a quasi-steady state in which the energy fluctuates around a mean value. Note that W_{chrom} is comparable to W_{cor}, even though the chromosphere represent only a small fraction of the loop volume. The coronal energy $W_{cor}(t)$ is

dominated by magnetic free energy, while $W_{\mathrm{chrom}}(t)$ is dominated by the kinetic energy of the plasma (see Figure 9(d)). Figure 10(b) shows similar plots for the volume integrated heating rates in the corona (black curve) and in the chromosphere (red curve). This figure demonstrates that most of the injected energy is dissipated in the corona, as expected for a magnetic braiding model. The main problem with this model is that the amount of energy involved is small compared to the radiative and conductive losses.

The above results may be compared with other magnetic braiding models. For example, Dahlburg et al. (2016) simulated magnetic braiding in a coronal loop, using a full MHD description of the plasma. The computational domain extends from the base of the TR at one end of the loop to the TR at the other end, and random footpoint motions with velocity $v_{\mathrm{rms}} = 1$ km s^{-1} are applied at the TR boundaries. The background magnetic field is assumed to be uniform, and different values of the magnetic field strength B_0 are considered (100, 200 and 400 G). The footpoint motions produce braided magnetic fields, and the associated field-aligned electric currents produce Ohmic heating of the coronal plasma. The authors simulate the response of the coronal plasma to such heating, and find that the heating produces large variations in coronal temperature across the loop, but only small density variations. Dahlburg et al. (2016) compare the simulated DEM distributions with observations, and find that a good fit to the observations is obtained for a coronal field strength of 400 G. However, the Dahlburg et al. model has several limitations that may cause the coronal heating rates and temperatures to be overestimated. First, the model does not include the chromosphere, which may cause the energy available to the corona to be overestimated. Second, the model does not take into account coronal loop expansion, and assumes a magnetic field strength of 400 G, which is high compared to the values typically found in extrapolations of photospheric magnetograms. For example, in our previous work on observed coronal loops in the cores of active regions we obtained minimum field strengths in the range 13 – 30 G (paper II), 30 – 120 G (paper III), and 20 – 45 G (paper IV). Finally, in the model by Dahlburg et al. (2016) the temperature and density are held fixed at the TR boundaries, so there is no chromospheric "evaporation" in response to coronal heating events. Therefore, the model may overestimate the temperature increase resulting from a given heating event.

6. DISCUSSION

In this paper we developed a model for the heating of a magnetic loop containing multiple flux tubes in the photosphere. The flux tubes merge at a height $z_m \approx 520$ km in the upper photosphere, so the magnetic field in the chromosphere and corona is a collection of flux tubes that are pressed up against each other. We simulated the dynamics of Alfvén waves in such a magnetic structure, using a reduced MHD model. The waves are assumed to be produced by random footpoint motions *inside* the photospheric flux tubes. The turbulent waves were simulated for a period of 3000 s, comparable to the loop cooling time (about 2000 s). We found that AWT can produce enough heat to maintain a coronal pressure $p_{\mathrm{cor}} = 1.8$ dyne cm^{-2} and peak temperature $T_{\mathrm{max}} = 2.5$ MK. The wave heating rate Q varies strongly in space and time, but the time-averaged rate $\overline{Q}$ in the corona is nearly constant over the loop cross-section, so the model does not predict large temperature or density variations across the loop. In contrast, the observed DEM distributions indicate that active regions have broad temperature distributions with peak temperatures of 3 – 4 MK but extending to significantly higher and lower temperatures (e.g., Winebarger et al. 2011; Warren et al. 2011, 2012). Therefore, the value

of $T_{\max}$ predicted by our AWT model is not quite high enough, and the model cannot readily explain the observed broad DEM distributions.

We simulate the effects of AWT on the Doppler shift and Doppler broadening of spectral lines formed in the corona (section 4.5). We predict that the Alfvén waves should be detectable as variations in Doppler shift, provided the instrument has sufficiently high spatial resolution (FWHM < 0.5"). The rms value of the non-thermal velocity is predicted to be nearly independent of spatial resolution, and is about 27 km s^{-1}, which is high compared to the observed values (Brooks & Warren 2016; Testa et al. 2016; Hara & Ichimoto 1999). Therefore, despite not providing enough heating, the AWT model is already injecting as much energy into the corona as is consistent with spectroscopic observations.

The heating rates $Q(t)$ for co-moving points vary strongly with time, and can be described as a series of heating events. The integrated energy $\int Q(t)dt$ of an event can be compared with the thermal energy density of the plasma. In the chromosphere the bursts have enough energy to significantly increase the temperature, which may be important for understanding type II spicules and other dynamic phenomena in the chromosphere (De Pontieu et al. 2007). However, in the corona the bursts have only modest energy compared to the thermal energy density of the coronal plasma, and the temperature fluctuations produced by such bursts are predicted to be relatively small (see section 4.4). The observations indicate there are large changes in temperature as the loops heat up and cool (e.g., Viall & Klimchuk 2011, 2012). Our model cannot directly explain such observations.

The model predicts that the time-averaged heating rate $\overline{Q}$ is enhanced at the boundaries between the flux tubes in the chromosphere (these boundaries are separatrix surfaces in our model). In the region just above the merging height the spatially averaged heating rate Q_{tot} is enhanced by about a factor 2 compared to its value just below the merging height. However, this extra heating at the flux tube boundaries does not extend to large heights. The reason for this rapid decline with height of the boundary heating is that the waves in the chromosphere are quite turbulent, and produce large displacements of the boundary surfaces. Therefore, the extra energy associated with the discontinuities in the velocity field at the merging height is quickly dissipated.

In our first model (section 4) we assumed that the photospheric flux tubes have fixed positions, so we did not take into account the observed random motions of magnetic flux elements at the solar surface (e.g., Wang 1988; Schrijver & Martin 1990; Muller et al. 1994; Schrijver et al. 1996; Berger et al. 1998; Hagenaar et al. 1999; Abramenko et al. 2011). To estimate the effects of such random motions on coronal heating, we presented (in section 5) a second model in which the flux tubes are omitted and the footpoint motions applied directly at the merging heights. The imposed random motions have a correlation time $\tau_c \approx 400$ s, and have a random walk diffusion constant of about 200 km^2 s^{-1}, which is at the high end of the observed range of photospheric diffusion constants (see Berger et al. 1998, and references therein). In this "magnetic braiding" model the footpoint motions produce quasi-static braiding of the coronal field lines. We find that the model without photospheric flux tubes and long correlation time produces much less coronal heating than the AWT model with flux tubes. We conclude that the observed random motions on times scales longer than a few minutes are not the main source of energy for coronal heating in active regions. The short-period waves inside the flux tubes appear to be more important for the energy balance of the coronal plasma.

The models described in this paper lack the kind of impulsivity usually required to explain the observed characteristics of the coronal plasma. To have more impulsive heating would require that magnetic free energy builds up in the corona over a period of several hours before the energy is released

by a reconnection event (e.g., Parker 1983; Pontin & Hornig 2015). However, we find that such energy build-up does not occur in either of our models. In the AWT model the counter-propagating waves interact so strongly that the wave energy is dissipated on a time scale of only about 100 s, too small for significant energy build-up to occur. In the magnetic braiding model the dissipation time is much longer ($\sim 10^4$ s), but we find that the amount of energy released is simply too small to explain the observed coronal temperatures. Therefore, we do not find the conditions necessary to produce strong heating events. In nanoflare heating models (see reviews by Klimchuk 2010; Cargill et al. 2015), the magnitude of a coronal heating event is a free parameter that can be adjusted to obtain agreement with solar observations. However, in our simulation study only the footpoint motions can be imposed, and the magnitude of heating events cannot be adjusted. Our models use realistic coronal field strengths and photospheric footpoint motions, so we believe our simulation results put important constraints on the magnitudes of heating events that can be produced by the observed footpoint motions.

As mentioned above, the AWT model described in section 4 cannot readily explain the observed broad DEM distributions of active regions. In the remainder of this section we discuss several possibilities for resolving this problem. First, the present model may underestimate the amount of energy injected into the coronal part of the loop. The flux tubes are modeled using the zeroth order thin-tube approximation, which is not very accurate at larger heights in the photosphere (Yelles Chaouche et al. 2009). The merging of flux tubes is described in a simple way (see Figure 1), which does not accurately represent the complex 3D magnetic structure of a plage region (Buehler et al. 2015). Potential-field modeling suggests that the transverse velocities in the chromosphere may be enhanced by the presence of magnetic nulls at the merging height (van Ballegooijen et al. 1998; van Ballegooijen & Hasan 2003), but the present model does not include such null points.

Another limitation of the present modeling is that it is based on the so-called reduced MHD approximation, so it does not take into account flows along the background magnetic field or density variation across the field lines. It is well known that in the upper chromosphere and TR there are strong flows along the field lines in the form of jets and spicules (e.g. Beckers 1972; Sterling 2000; De Pontieu et al. 2007; Tian et al. 2014), and such flows may in fact be caused by localized heating and/or wave pressure forces in the chromosphere (e.g., Murawski et al. 2015; Cranmer & Woolsey 2015). Therefore, some of the wave energy may be channeled into parallel flows, which is not taken into account in the present model. The jet-like flows cause the TR to be highly corrugated, with large variations in density across the field lines (Feldman et al. 1997; Zhang et al. 1998; Peter 2013). Therefore, the present version of the AWT model may overestimate the degree of wave reflection at the TR, and underestimate the amount of energy transmitted into the corona. To address this problem full 3D MHD simulations of coronal loops and their connections to the lower atmosphere are needed. Such simulations are very challenging because of the high spatial and temporal resolution required in the corrugated TRs.

The strength of the magnetic disturbances at the footpoints of the hot loops may have been underestimated. During the growth phase of active regions, new magnetic flux emerges into the solar atmosphere from the convection zone below, and the newly emerged field is generally not aligned with the preexisting field (e.g., Ortiz et al. 2014). The mis-alignment angles may be 10 – 20 degrees, significantly larger than the values predicted by the models presented in this paper. Magnetic reconnection between the old and new flux systems could produce some or all of the observed high

temperature emission. The role of flux emergence in producing the observed DEM distributions should be further investigated. Also, some hot loops may be anchored in sunspot penumbrae, which are known to have different orientation angles of the magnetic fields in bright and dark penumbral filaments (see review by Borrero & Ichimoto 2011). These complex penumbral fields could cause more magnetic energy to be injected into the corona. However, not all hot loops are connected to sunspot penumbrae.

Finally, the model may overestimate the rate of cooling of the coronal plasma. In standard loop models the thermal conductivity is assumed to be dominated by Coulomb collisions, and is given by Spitzer's formula (Cohen et al. 1950; Spitzer & Härm 1953; Spitzer 1962). The effects of wave turbulence on pitch-angle scattering of non-thermal and thermal electrons have recently been considered in the context of solar flares to explain the observed rates of temperature decrease in post-flare loops (Kontar et al. 2014; Bian et al. 2016a,b). We suggest that similar effects of pitch-angle scattering may occur in non-flaring loops, producing a reduction in the thermal conductivity compared to Spitzer's value. In preliminary modeling using different values of the conductivity parameter κ_0, we have found that reducing this parameter by a factor $3-5$ allows the AWT model to reproduce the observed temperatures in the range $3-4$ MK. However, a simple reduction of κ_0 may not be the best way to describe the effects of plasma turbulence. Such a reduction of the thermal conductivity would also affect the thermal stability of coronal loops (e.g., Mikić et al. 2013; Lionello et al. 2013), and may play a role in the formation of coronal rain (Antolin & Rouppe van der Voort 2012; Antolin et al. 2015).

APPENDIX

A. NUMERICAL METHODS

The numerical methods used in the present work are similar to those used in simulating Alfvén waves in the solar wind (see paper V). The waves are described using stream functions $f_\pm(x, y, s, t)$ for the Elsasser variables. The dependence of these functions on the perpendicular x and y coordinates are described as follows:

$$f_\pm(x, y, s, t) = \sum_{k=1}^{M} f_{\pm,k}(s, t) F_k(\tilde{x}, \tilde{y}), \tag{A1}$$

where $\tilde{x}$ and $\tilde{y}$ are dimensionless perpendicular coordinates, $F_k(\tilde{x}, \tilde{y})$ is an eigenfunction of the $\nabla_\perp^2$ operator, k is an index enumerating the different eigenfunctions, M is the number of eigenmodes, and $f_{\pm,k}(s, t)$ are the mode amplitudes describing the waves. Two different sets of eigenfunctions are used, one for the flux tubes and another for the merged field. For the flux tubes we use $\tilde{x} \equiv x/R(s) + 0.5$ and $\tilde{y} \equiv y/R(s) + 0.5$, where $R(s)$ equals the width of a flux tube, $R(s) = w_t(s)$, so the dimensionless coordinates are in the range $0 \le \tilde{x} \le 1$ and $0 \le \tilde{y} \le 1$. The eigenfunctions satisfy "closed" boundary

conditions with $F_k = 0$ at the side boundaries of the tubes, so they are products of sine functions:

$$F_k(\tilde{x}, \tilde{y}) \equiv F_{n_x, n_y}(\tilde{x}, \tilde{y}) = 2\sin(n_x\pi\tilde{x})\sin(n_y\pi\tilde{y}). \qquad (A2)$$

For flux tubes n_x and n_y are integers in the range 1 to 42, so there are $M = 1764$ eigenmodes, and equation (A1) is equivalent to a 2-dimensional (2D) sine transform. For the merged field we use $\tilde{x} \equiv x/R(s)$ and $\tilde{y} \equiv y/R(s)$, where $R(s) = w_m(s)/2$ is the half-width of the computational domain, so the dimensionless coordinates are in the range $0 \le \tilde{x} \le 2$ and $0 \le \tilde{y} \le 2$. Also, we use periodic boundary conditions, so the eigenfunctions are products of sine and cosine functions, and equation (A1) is now equivalent to an ordinary 2D Fourier transform (for the merged field $M = 29{,}240$). Each eigenmode has a well-defined dimensionless wavenumber a_k (in units of $1/R$), and the maximum wavenumber in one direction is $a_{\max} = 42\pi$ for flux tubes and $a_{\max} = 85\pi$ for the merged field.

Inserting equation (A1) into the reduced MHD equations (10), we find

$$\begin{aligned}
\frac{\partial\omega_{\pm,k}}{\partial t} = {}&\mp v_A\frac{\partial\omega_{\pm,k}}{\partial s} + \frac{1}{2}\frac{dv_A}{ds}(\omega_{+,k} - \omega_{-,k}) \\
&+ \frac{1}{2R^4}\sum_j\sum_i M_{kji}(a_i^2 - a_j^2 - a_k^2)f_{\pm,j}f_{\mp,i} - \nu_{\pm,k}\,\omega_{\pm,k},
\end{aligned} \qquad (A3)$$

where $\omega_{\pm,k}(s,t)$ is the wave vorticity for each mode. The four terms on the right-hand side describe wave propagation, linear couplings (including wave reflection), nonlinear couplings, and wave damping. Here M_{kji} is a dimensionless coupling matrix (see equation (5) in paper V), and the damping rates $\nu_{\pm,k}(s,t)$ are discussed below. The nonlinear terms are evaluated using Fourier Transform methods. For each position s along the loop, the quantities inside the bracket operators in equation (10) are computed by transforming these quantities from the spectral to the spatial domain, where the brackets are easily evaluated. Then the results are transformed back to the spectral domain to determine the nonlinear term in equation (A3). For the merged field the transformation involves a spatial grid of 256×256 points. For flux tubes the sine transform is performed as an ordinary Fourier transform on a grid twice the width of one flux tube (128×128 grid), and the calculation is done separately for each flux tube.

The coupled equations (A3) are solved by using finite differences in the coordinate s along the background field. To accurately describe the wave reflections at the TRs, we use a highly non-uniform grid, s_n, where n is an index of the grid points. In the TRs the steps Δs_n between neighboring grid points must be very small (less than 1 km), which means that the Alfvén travel time $\Delta t_n = \Delta s_n/v_{A,n}$ between grid points is also very small (less than 1 ms). Therefore, to properly simulate the dynamics of the waves it is necessary to take very small time steps at those heights. Elsewhere along the loop the variations in the background atmosphere are more gradual and we can take larger time steps (up to 1 s). We developed a method for dealing with different time steps in different regions along the loop. Let Δt_0 be the maximum time step to be used (for the models presented in this paper $\Delta t_0 = 0.811$ s). The grid s_n is chosen such that the Alfvén travel time Δt_n is constant within certain sections of the grid, and jumps by a factor 2 between sections. Therefore, within each section $\Delta t_n = \Delta t_0 2^{-N}$, where N is the level of refinement for that section ($0 \le N \le 14$). Furthermore, within each section we use a time step Δt equal to the wave travel time Δt_n between grid points. Let $\omega_{\pm,n}$ and $\omega_{\pm,n+1}$ be the vorticities of the waves at grid points n and $n + 1$ at time t, where we

omit the dependence on mode index k. Then the vorticities at time $t + \Delta t$ are given by

$$\omega'_{+,n+1} = (1 + \epsilon_n)\omega_{+,n} - \epsilon_n\omega_{-,n+1}, \tag{A4}$$
$$\omega'_{-,n} = \epsilon_n\omega_{+,n} + (1 - \epsilon_n)\omega_{-,n+1}, \tag{A5}$$

where $\epsilon_n \equiv (v_{A,n+1} - v_{A,n})/(v_{A,n+1} + v_{A,n})$ is related to the gradient in Alfvén speed. To evolve the waves over a full time step Δt_0 the sections of the grid with refinement level N must be processed 2^N times, so highly refined sections are processed much more frequently. The order in which the different sections are processed is such that all sections evolve more or less equally in time, with no more than one time step Δt_n between neighboring sections. The nonlinear and damping terms in the reduced MHD equations are evaluated only at the full time steps Δt_0. We find that this technique produces reasonably accurate results for the propagation and reflection of waves in the TR.

For the AWT model the footpoint motions are imposed at the bottom of the flux tubes, $s = 0$ and $s = L$. The vorticities $\tilde{\omega}_k(t)$ of the three driver modes are computed as described in section 3.5, and for all other modes we set $\tilde{\omega}_k(t) = 0$. The boundary conditions are implemented by setting the amplitudes of the upward propagating waves as follows:

$$\omega_{+,k}(t) = 2\tilde{\omega}_k(t) - \omega_{-,k}(t) \quad \text{at } s = 0, \tag{A6}$$

and similar for the waves $\omega_{-,k}(t)$ at $s = L$. Equation (A6) implies that the downward propagating waves in the flux tubes are strongly reflected at the base of the photosphere, but this is not a problem in the AWT model because the waves are quite turbulent and no standing waves are created. However, for the magnetic braiding model the footpoint motions are applied at the merging heights, and we find that equation (A6) leads to the formation of a standing wave that resonates between the merging height and the TR. This wave has a period $P \approx 70$ s. To suppress this standing wave, we modify equation (A6) as follows:

$$\omega_{+,k}(t) = 2\tilde{\omega}_k(t) - \tfrac{1}{2}\left[\omega_{-,k}(t) + \omega_{-,k}(t - \tfrac{1}{2}P)\right] \quad \text{at } s = z_m, \tag{A7}$$

and similar for the wave $\omega_{-,k}(t)$ at $s = L - z_m$. Equation (A7) implies that a downward propagating wave with period P is transmitted at the merging height, while longer-period waves are reflected. Therefore, the imposed footpoint motions, which have a correlation time of about 400 s, are almost unaffected by this modification of the boundary conditions in the magnetic braiding model.

The term in equation (10) involving the viscosity $\tilde{\nu}_\pm$ produces a wave damping rate $\nu_{\pm,k}$ given by

$$\nu_{\pm,k} = \nu_\pm \left(\frac{a_k}{a_{\max}}\right)^2, \tag{A8}$$

where $\nu_\pm \equiv \tilde{\nu}_\pm(a_{\max}/R)^2$. This rate depends quadratically on wavenumber, which is different from the "hyperdiffusion" used in our earlier work (papers I through IV). The use of ordinary diffusion is made possible by the fact that we now have much higher spatial resolution in x and y compared to our earlier models. Most of the wave damping occurs at high wavenumbers, $a_k > (2/3)a_{\max}$, which we call the dissipation range. The maximum damping rates $\nu_\pm(s, t)$ are chosen such that the wave damping time is comparable to the cascade time scale. For the AWT model (section 4) we set $\nu_\pm = 1.5k_dZ_{\mp,d}$, where $k_d = (2/3)a_{\max}/R$ is the wavenumber at the start of the dissipation range,

and $Z_{\mp,d}$ are the Elsasser variables just below this range. The latter are given by sums over all modes with wavenumbers in the range $(1/2)a_{\max} < a_k < (2/3)a_{\max}$ [see equation (23) in paper V]. The damping rates $\nu_\pm(s,t)$ are also smoothed in time, using a running time average with time constant of 500 s. For the magnetic braiding model (section 5) the Elsasser variables are dominated by magnetic fluctuations, so we use $\nu_+ = \nu_- = 1.5 k_d V_d$, where V_d is the total velocity of modes in the above wavenumber range.

The energy dissipation rates averaged over the loop cross-section can be computed by adding the contributions from all wave modes:

$$Q_\pm(s,t) = \frac{\rho}{2} \sum_{k=1}^{M} \nu_{\pm,k} \left(\frac{a_k}{R}\right)^2 f_{\pm,k}^2 = \frac{\rho \nu_\pm}{2R^2 a_{\max}^2} \sum_{k=1}^{M} a_k^4 f_{\pm,k}^2, \tag{A9}$$

and below the merging heights these quantities are further averaged over all flux tubes. The total energy dissipation rate is $Q_{\text{tot}}(s,t) \equiv Q_+ + Q_-$. Position dependent dissipation rates are computed as follows:

$$Q_\pm(x,y,s,t) = \frac{1}{2} \rho \nu_\pm \left(\frac{R}{a_{\max}}\right)^2 \left(S_{\pm,xx}^2 + S_{\pm,xy}^2\right), \tag{A10}$$

where $S_{\pm,xx}$ and $S_{\pm,xy}$ are the diagonal and off-diagonal components of the rate of strain tensor for the Elsasser variables:

$$S_{\pm,xx}(x,y,s,t) \equiv 2 \frac{\partial z_{\pm,x}}{\partial x} = 2 \frac{\partial^2 f_\pm}{\partial x \partial y}, \tag{A11}$$

$$S_{\pm,xy}(x,y,s,t) \equiv \frac{\partial z_{\pm,y}}{\partial x} + \frac{\partial z_{\pm,x}}{\partial y} = \frac{\partial^2 f_\pm}{\partial y^2} - \frac{\partial^2 f_\pm}{\partial x^2}. \tag{A12}$$

Using the orthogonality of the eigenmodes, it can be shown that the average of equation (A10) over the loop cross-section equals expression (A9). The position dependent rates are determined by first computing $S_{\pm,xx}$ and $S_{\pm,xy}$ in the spectral domain, and then Fourier transforming them to the spatial domain. The total dissipation rate shown in Figure 6 is given by $Q(x,y,s,t) = Q_+ + Q_-$.

B. CORONAL LOOP MODEL

The background atmosphere for the reduced MHD model is constructed by solving the energy balance equations for a coronal loop. We consider a thin magnetic flux tube with length L_c in the corona, as measured from the base of the TR at one end of the loop to the base of the TR at the other end. The cross-sectional area $A_0(s)$ of the tube is an arbitrary function of position s along the loop, and is related to the magnetic field strength $B_0(s)$ such that $A_0(s)B_0(s) = \Phi = $ constant. We assume that the plasma heating is either steady in time or fluctuates on a time scale much shorter than the loop cooling time (high-frequency heating). Furthermore, variations in heating rate across the loop are neglected. Then the heating rate $Q_A(s)$ can be taken to be constant in time. The coronal loop is assumed to be thermally stable, so the temperature $T(s)$ and density $\rho(s)$ are also constant in time. The model can also describe asymmetric loops, so there may be a steady mass flow along the loop with velocity $v(s)$. For the purpose of this Appendix the endpoints of the loop are assumed to be located at $s = 0$ and $s = L_c$, where L_c is the coronal loop length. These endpoints are defined as those points in the TR where the temperature equals twice the chromospheric temperature, $T(0) = T(L_c) = 2T_0$,

where $T_0 = 8000$ K. The gas pressure $p(s)$, mass density $\rho(s)$ and electron density $n_e(s)$ are given by the ideal gas law:

$$p = c_1 n_p k_B T, \quad \rho = c_2 m_p n_p, \quad n_e = c_3 n_p, \tag{B13}$$

where $n_p(s)$ is the proton density, m_p is the proton mass, and k_B is the Boltzmann constant. The plasma is assumed to be fully ionized. The constants c_i are given by $c_1 = 2 + 3A_{He}$, $c_2 = 1 + 4A_{He}$, and $c_3 = 1 + 2A_{He}$, where $A_{He} = 0.1$ is the helium abundance. For simplicity we neglect the effects of gravity in the corona, and we assume that the flow velocity is small compared to the sound speed. Then the gas pressure $p(s) = p_{cor} =$ constant. The coronal pressure p_{cor} is treated as a free parameter of the model. In the following we assume $B_0(s)$, L_c and p_{cor} to be known quantities.

In steady state the wave heating rate $Q_A(s)$ is balanced by radiative and conductive losses:

$$B_0 \frac{d}{ds}\left(\frac{F}{B_0}\right) = Q_A(s) - n_e^2 \Lambda(T), \tag{B14}$$

where $F(s)$ is the sum of conductive and enthalpy fluxes:

$$F(s) = -\kappa(T)\frac{dT}{ds} + 2.5\mu_0 B_0 c_1 k_B(T - T_0). \tag{B15}$$

Here $\mu_0 \equiv n_p v/B_0$ is the proton flux per unit magnetic flux, which is constant along the loop. The radiative loss function $\Lambda(T)$ is taken from CHIANTI version 8 (Dere et al. 1997; DelZanna et al. 2015a), assuming coronal abundances (Schmelz et al. 2012). In the corona the thermal conductivity $\kappa(T)$ is dominated by the electrons (Spitzer 1962), but in the TR there is an important contribution from ambipolar diffusion, i.e., the upward diffusion of neutrals and downward diffusion of ions and electrons (Fontenla et al. 1990, 1991). In this paper we use the following expression for the total conductivity:

$$\kappa(T) = \kappa_0 T^{5/2} + \frac{\kappa_1}{T}\left[1 + \left(\frac{T}{10^4\ \text{K}}\right)^{-5}\right], \tag{B16}$$

where $\kappa_0 = 10^{-6}$ erg cm^{-1} s^{-1} K$^{-7/2}$ is the Spitzer conductivity, and the second term with $\kappa_1 = 5 \times 10^9$ erg cm^{-1} s^{-1} is an approximation for the contribution from ambipolar diffusion (based on Figure 7 in Fontenla et al. 1991). The heating rate is assumed to be of the form given in equation (17). Then equation (B14) can be integrated as follows:

$$\frac{F(s)}{B_0(s)} = \frac{F(0)}{B_0(0)} + c_0 \int_0^s [B_0(s)]^{n-1} ds - \int_0^s \frac{n_e^2 \Lambda(T)}{B_0(s)} ds. \tag{B17}$$

Using $s = L_c$, we obtain an expression for c_0 in terms of two integrals along the coronal loop and values of the fluxes $F(0)$ and $F(L_c)$ at the two endpoints. Given an estimate for the coronal temperature $T(s)$ and pressure p_{cor}, both integrals can be readily computed. The endpoint fluxes are computed as described in the Appendix of Schrijver & van Ballegooijen (2005). Therefore, equation (B17) with $s = L_c$ yields the value of c_0, which can be used to derive the heating rate $Q_A(s)$ and total energy flux $F(s)$. Similarly, equation (B15) can be integrated to yield

$$\int_0^s F(s) ds = -\int_{T(0)}^{T(s)} \kappa(T) dT + 2.5\mu_0 c_1 k_B \int_0^s B_0(s)[T(s) - T_0] ds, \tag{B18}$$

and using $s = L_c$ we find an expression for mass flow parameter μ_0. Here we use the fact that the temperatures at the two endpoints are equal, $T(0) = T(L_c) = 2T_0$, so the integral over the conductive flux vanishes when integrating along the entire loop. Finally, we obtain the quantity $\int_{T(0)}^{T(s)} \kappa(T) dT$ as a function of s from equation (B18), which can be inverted to obtain a new estimate for the temperature $T(s)$. We repeat this process until the relative changes in temperature are less than 0.1% everywhere along the loop.

REFERENCES

Abramenko, V.I., Carbone, V., Yurchyshyn, V., et al. 2011, ApJ, 743, 133

Alfvén, H., 1947, MNRAS, 107, 211

Antolin, P., & Rouppe van der Voort, L. 2012, ApJ, 745, 152

Antolin, P., & Shibata, K. 2010, ApJ, 712, 494

Antolin, P., Shibata, K., Kudoh, T., Shiota, D., & Brooks, D. 2008, ApJ, 688, 669

Antolin, P., Vissers, G., Pereira, T. M. D., Rouppe van der Voort, L., & Scullion, E. 2015, ApJ, 806, 81

Arregui, I. 2015, Phil. Trans. R. Soc. A 373, 20140261, http://dx/doi.org/10.1098/rsta.2014.0261

Aschwanden, M. 2005, Physics of the Solar Corona (Springer: Berlin)

Asgari-Targhi, M., & van Ballegooijen, A.A. 2012, ApJ, 746, 81 (paper II)

Asgari-Targhi, M., van Ballegooijen, A.A., Cranmer, S.R., & DeLuca, E.E. 2013, ApJ, 773, 111 (paper III)

Asgari-Targhi, M., van Ballegooijen, & Imada, S. 2014, ApJ, 786, 28 (paper IV)

Asgari-Targhi, M., Schmelz, J. T., Imada, S., Pathak, S., & Christian, G. M. 2015, ApJ, 807, 146

Bale, S. D., Kellogg, P. J., Mozer, F. S., Horbury, T. S., & Reme, H. 2005, Phys. Rev. Letters, 94, 215002

Beckers, J. M. 1972, ARA&A, 10, 73

Belcher, J.W. 1971, ApJ, 168, 509

Berger, T. E., & Title, A. M. 1996, ApJ, 463, 365

Berger, T. E., & Title, A. M. 2001, ApJ, 553, 449

Berger, T. E., Löfdahl, M. G., Shine, R. A., & Title, A. M. 1998, ApJ, 506, 439

Berger, T. E., Rouppe van der Voort, L. H. M., Löfdahl, M. G., Carlsson, M., Fossum, A., Hansteen, V. H., Marthinussen, E., Title, A., & Scharmer, G. 2004, A&A, 428, 613

Berger, M. A. 1991, A&A, 252, 369

Berger, M. A. 1993, Phys. Rev. Lett., 70, 705

Berger, M. A., & Asgari-Targhi, M. 2009, ApJ, 705, 347

Berger, M. A., Asgari-Targhi, M., & DeLuca, E. E. 2015, J. Plasma Phys., 81, 395810404

Bian, N. H., Kontar, E. P., & Emslie, A. G. 2016, ApJ, 824, 78

Bian, N. H., Watters, J., M., Kontar, E. P., & Emslie, A. G. 2016, ApJ, 833, 76

Bingert, S., & Peter, H. 2011, A&A, 530, A112

Borovsky, J. E. 2012, J. Geophys. Res., 117, A05104

Borrero, J. M., & Ichimoto, K. 2011, Living Rev. Solar Phys., 8, 4, http://www.livingreviews.org/lrsp-2011-4

Bourdin, Ph.-A., Bingert, S., & Peter, H. 2015, A&A, 580, A72

Brooks, D. H., Warren, H. P., Ugarte-Urra, I., & Winebarger, A. R. 2013, ApJL, 772, L16

Brooks, D. H., & Warren, H. P. 2016, ApJ, 820, 63

Brosius, J. W., Davila, J. M., Thomas, R. J., et al. 1996, ApJS, 106, 143

Bruls, J. H. M. J., & Solanki, S. K. 1995, A&A, 293, 240

Buehler, D., Lagg, A., Solanki, S. K., & van Noort, M. 2015, A&A, 576, A27

Cargill, P. 1994, ApJ, 422, 381

Cargill, P. J., Warren, H. P., & Bradshaw, S. J. 2015, Phil. Trans. R. Soc. A 373, 20140260, http://dx/doi.org/10.1098/rsta.2014.0260

Cargill, P., & Klimchuk, J. A. 1997, ApJ, 478, 799

Cargill, P., & Klimchuk, J. A. 2004, ApJ, 605, 911

Chandran, B. D. G., Dennis, T. J., Quataert, E., & Bale, S. D. 2011, ApJ, 743, 197

Chitta, L.P., van Ballegooijen, A.A., Rouppe van der Voort, L., DeLuca, E. E., & Kariyappa, R. 2012, ApJ, 752, 48

Cho, J., Lazarian, A., & Vishniac, E. T. 2002, ApJ, 564, 291

Cohen, R. S., Spitzer, L., Jr. & Routly, P. M. 1950, Phys. Rev., 80, 230

Coleman, P. J., Jr. 1968, ApJ, 153, 371

Cranmer, S.R., Asgari-Targhi, M., Miralles, M. P., Raymond, J. C., Strachan, L., Tian, H., & Woolsey, L. N. 2015, Phil. Trans. Royal Soc. A, 373, 20140148

Cranmer, S. R., & Woolsey, L. N. 2015, ApJ, 812, 71

Cranmer, S. R., van Ballegooijen, A. A., & Edgar, R. J. 2007, ApJS, 171, 520

Dahlburg, R. B., Einaudi, G., Taylor, B. D., Ugarte-Urra, I., Warren, H. P., Rappazzo, A. F., & Velli, M. 2016, ApJ, 817, 47

Defouw, R. J. 1976, ApJ, 209, 266

De Groof, A., & Goossens, M. 2002, A&A, 386, 691

DelZanna, G., Dere, K. P., Young, P. R., Landi, E., & Mason, H. 2015a, A&A, 582, A56

DelZanna, G., Tripathi, D., Mason, H., Subramanian, S., & O'Dwyer, B. 2015b, A&A, 573, A104

De Moortel, I., & Browning, Ph. 2015, Phil. Trans. R. Soc. A 373, 20140269, http://dx/doi.org/10.1098/rsta.2014.0269

De Pontieu, B., McIntosh, S. W., Carlsson, M., et al. 2007, Sci, 318, 1574

Dere, et al. 1997, A&AS, 125, 149

DeVore, C. R., Sheeley, N. R., Jr., Boris, J. P., Young, T. R., Jr., & Harvey, K., 1985, SoPh, 102, 41

Dmitruk, P., & Matthaeus, W. H. 2003, ApJ, 597, 1097

Doschek, G. A. 2012, ApJ, 754, 153

Doschek, G. A., Mariska, J. T., Warren, H. P., Brown, C. M., Culhane, J. L. , Watanabe, T., Young, P. R., & Mason, H. E. 2007, ApJL, 667, L109

Elsasser, W. M. 1950, Phys. Rev., 79, 183

Feldman, U., Doschek, G. A., & Mariska, J. T. 1979, ApJ, 229, 369

Fischer, C. E., de Wijn, A. G., Centeno, R., Lites, B.. W., & Keller, C. U. 2009, A&A, 504, 583

Fletcher, L., & de Pontieu, B. 1999, ApJL, 520, L135

Fludra, A., Hornsey, C., & Nakariakov, V. M. 2017, ApJ, 834, 100

Fontenla, J. M., Avrett, E. H., & Loeser, R. 1990, ApJ, 355, 700

Fontenla, J. M., Avrett, E. H., & Loeser, R. 1991, ApJ, 377, 712

Galsgaard, K., & Nordlund, Å 1996, J. Geophys. Res., 101, 13445

Goldreich, P., & Sridhar, S. 1995, ApJ, 438, 763

Goossens, M., Andries, J., Soler, R., et al. 2012, ApJ, 753, 111

Goossens, M., Erdélyi, R., Ruderman, M.S. 2011, SSRv, 158, 289

Goossens, M., Van Doorsselaere, T., Soler, R., & Verth, G. 2013, ApJ, 768, 191

Gudiksen, B. V., & Nordlund, Å 2005, ApJ, 618, 1020

Hagenaar, H. J., Schrijver, C. J., Title, A. M., &b Shine, R., A. 1999, ApJ, 511, 932

Hara, H., & Ichimoto, K. 1999, ApJ, 513: 969

Hara, H., et al. 2008, ApJ, 678, L67

Heyvaerts, J., & Priest, E.R. 1983, A&A, 117, 220

Hollweg, J. V. 1978, SoPh, 56, 305

Hollweg, J. V. 1986, J. Geophys. Res., 91, 4111

Hollweg, J. V., Jackson, S., & Galloway, D. 1982, SoPh, 75, 35

Ichimoto, K., Hara, H., Takeda, A., Kumagai, K., Sakurai, T., Shimizu, T., & Hudson, H. S. 1995, ApJ, 445, 978

Iroshnikov, P. S. 1963, Astron. Zh., 40, 742 (English translation in Sov. Astron. 7, 566 [1964])

Janse, A. M., Low, B. C., & Parker, E. N. 2010, Phys. Plasmas, 17, 092901

Kano, R., & Tsuneta, S. 1996, PASJ, 48, 535

Klimchuk, J. A. 2000, SoPh, 193, 53

Klimchuk, J. A. 2006, SoPh, 234, 41

Klimchuk, J. A. 2010, in ASP Conf. Ser. 415, Proc. of Second Hinode Science Meeting, ed. B. Lites et al. (San Francisco: ASP), 221

Komm, R. W., Howard, R. F., & Harvey, J. W. 1995, SoPh, 158, 213

Kontar, E. P., Bian, N. H., Emslie, A. G., & Vilmer, N. 2014, ApJ, 780, 176

Kraichnan, R. H. 1965, Phys. Fluids, 8, 1385

Kudoh, T., & Shibata, K. 1999, ApJ, 514, 493

Lionello, R., Winebarger, A. R., Mok, Y., Linker, J. A., & Mikić, Z. 2013, ApJ, 773, 134

López-Fuentes, M., Klimchuk, J. A., & Démoulin, P. 2006, ApJ, 639, 459

López-Fuentes, M., Démoulin, P., & Klimchuk, J. A. 2008, ApJ, 673, 586

López-Fuentes, M., & Klimchuk, J. A. 2015, ApJ, 828, id.86

López-Fuentes, M., & Klimchuk, J. A. 2016, ApJ, 799, id.128

Manso Sainz, R., Martínez González, M. J., & Asensio Ramos, E. 2011, A&A, 531, L9

Maron, J., & Goldreich, P. 2001, ApJ, 554, 1175

Martens, P. C. H., Kankelborg, C. C., & Berger, T. E. 2000, ApJ, 537, 471

Martínez Pillet, V., Lites, B. W., & Skumanich, A. 1997, ApJ, 474, 810

Matthaeus, W. H., Goldstein, M. L., & Roberts, D. A. 1990, JGR, 95, 20673

Matthaeus, W. H., Zank, G. P., Oughton, S. Mullan, D. J., & Dmitruk, P. 1999, ApJ, 523, L93

Matsumoto, T., & Shibata, K. 2010, ApJ, 710, 1857

McIntosh, S. W., De Pontieu, B., & Tarbell, T. D. 2008, ApJ, 673, L219

McIntosh, S. W., De Pontieu, B., Carlsson, M., Hansteen, V., Boerner, P., & Goossens, M. 2011, Nature, 475, 477

Mercier, C., & Trottet, G. 1997, ApJ, 474, L65

Mikić, Z., Schnack, D. D., & van Hoven, G. 1989, ApJ, 338, 1148

Mikić, Z., Lionello, R., Mok, Y., Linker, J. A., & Winebarger, A. R. 2013, ApJ, 773, 94

Moriyasu, S., Kudoh, T., Yokoyama, T., & Shibata, K. 2004, ApJ, 601, L107

Morton, R. J., Tomczyk, S., & Pinto, R. 2015, Nat. Comm., DOI: 10.1038/ncomms8813

Muller, R., Roudier, T., Vigneau, J. & Auffret, H. 1994, A&A, 283, 232

Mumford, S. J., Fedun, V., & Erdélyi, R. 2015, ApJ, 799, 6

Murawski, K., Solovev, A. Musielak, K. et al. 2015, A&A, 577, A126

Nagata, S., Tsuneta, S., Suematsu, Y., et al. 2008, ApJ, 677, L145

Nisenson, P., van Ballegooijen, A. A., de Wijn, A. G., & Sütterlin, P. 2003, ApJ, 587, 458

Ortiz, A., Bellot Rubio, L. R., Hansteen, V. H., De La Cruz Rodríguez, J., & Rouppe Van Der Voort, L. 2014, ApJ, 781, 126

Oughton, S., Matthaeus, W. H., Dmitruk, P., Milano, L. J., Zank, G. P., & Mullan, D. J. 2001, ApJ, 551, 565

Parnell, C. E., & De Moortel, I. 2012, Phil. Trans. R. Soc. A 370, 3217-3240

Parker, E. N. 1972, ApJ, 174, 499

Parker, E. N. 1978, ApJ, 221, 368

Parker, E. N. 1983, ApJ, 264, 642

Parker, E. N. 1988, ApJ, 330, 474

Pascoe, D. J., Hood, A. W., de Moortel, I., & Wright, A. N. 2012, A&A, 539, A37

Pascoe, D. J., Wright, A. N., & de Moortel, I. 2011, ApJ, 731, 73

Patsourakos, S., & Klimchuk, J. A. 2009, ApJ, 696, 760

Perez, J. C., & Chandran, B. D. G. 2013, ApJ, 776, 124

Peter, H. 2013, SoPh, 288, 531

Poedts, S., Goossens, M., & Kerner, W. 1990, ApJ, 360, 279

Pontin, D. I., & Hornig, G. 2015, ApJ, 805, 47

Pontin, D. I., Janvier, M., Tiwari, S. K., Galsgarrd, K., Winebarger, A. R., & Cirtain, J. W. 2017, ApJ, 837, 108

Priest, E. R., Heyvaerts, J. F., & Title, A. M. 2002, ApJ, 576, 533

Rappazzo, A., F., Velli, M., Einaudi, G., & Dahlburg, R. B. 2007, ApJ, 657, L47

Rappazzo, A., F., Velli, M., Einaudi, G., & Dahlburg, R. B. 2008, ApJ, 677, 1348

Rappazzo, A., F., Velli, M., & Einaudi, G. 2013, ApJ, 771, 76

Ritchie, M. L., Wilmot-Smith, A. L., & Hornig, G. 2016, ApJ, 824, id.19

Rosner, R., Tucker, W. H., & Vaiana, G. S. 1978, ApJ, 220, 643

Schekochihin, A. A., Cowley, S. C., Dorland, W., Hammett, G. W., Howes, G. G., Quatert, E., & Tatsuno, T. 2009, ApJS, 182, 310

Schmelz, J. T., Reames, D. V., von Steiger, R., & Basu, S. 2012, ApJ, 755, 33

Schrijver, C. J., & Martin, S. F. 1990, SoPh, 129, 95

Schrijver et al. 1996, ApJ, 468, 921

Schrijver et al. 1999, SoPh, 187, 261

Schrijver, C. J., & van Ballegooijen, A. A. 2005, ApJ, 630, 552

Schrijver, C. J., & Zwaan, C. 2000, *Solar and Stellar Magnetic Activity* (Cambridge University Press: Cambridge, UK)

Scullion, E., Rouppe van der Voort, L., Wedemeyer, S., & Antolin, P. 2014, ApJ, 797, 36

Shebalin, J. V., Matthaeus, W. H., & Montgomery, D. 1983, J. Plasma Phys., 29, 525

Sheeley, N. R., Jr. 1981, The overall structure and evolution of active regions, in *Solar Active Regions*, ed. Frank Q. Orrall (Colorado Associated University Press: Boulder, Colorado), p. 17

Solanki, S. 1993, Space Sci Rev, 63, 1

Spitzer, L., Jr., & Härm, R. 1953, Phys. Rev., 89, 977

Spitzer, L., Jr. 1962, *Physics of Fully Ionized Gases* (New York: John Wiley and Sons, Inc)

Spruit, H. C. 1976, SoPh, 61, 363

Spruit, H. C. 1979, SoPh, 50, 269

Stenflo, J. O. 1973, SoPh, 32, 41

Sterling, A. C. 2000, SoPh, 196, 79

Strauss, H.R. 1976, Phys. Fluids, 19, 134

Strauss, H. R. 1997, J. Plasma Phys., 57, 83

Suzuki, T. K., & Inutsuka, S.-I. 2005, ApJ, 632, L49

Testa, P, De Pontieu, B., & Hansteen, V. 2016, ApJ, 827, 99

Threlfall, J., De Moortel, I., McIntosh, S. W., & Bethge, C. 2013, A&A, 556, A124

Tian, H., DeLuca, E. E., Cranmer, S. R., et al. 2014, Science, 346, 1255711

Tian, H., McIntosh, S. W., Habbal, S. R., He, J. 2011, ApJ, 736, 130

Tian, H., McIntosh, S. W. , Xia, L. , He, J. , & Wang, X. 2012, ApJ, 748, 106

Tian, H., McIntosh, S. W. , Wang, T., Ofman, L., De Pontieu, B., Innes, D. E. , & Peter, H. 2012, ApJ, 759, 144

Tomczyk, S., & McIntosh, S. W. 2009, ApJ, 697, 1384

Tomczyk, S., McIntosh, S. W., Keil, S. L., et al. 2007, Sci, 317, 1192

Tripathi, D., Klimchuk, J. A., & Mason, H. E. 2011, ApJ, 740, 111

Tripathi, D., Mason, H. E., Dwivedi, B. N., Del Zanna, G., & Young, P. R. 2009, ApJ, 694, 1256

Utz, D., Hanslmeier, R., Muller, R., et al. 2010, A&A, 511, A39

van Ballegooijen, A. A. 1986, ApJ, 311, 1001

van Ballegooijen, A. A. 1988, in *Solar and Stellar Coronal Structure and Dynamics*, Proc. of the Ninth Sacramento Peak Summer Symposium, ed. R. C. Altrock (National Solar Observatory: Sunspot, NM 88349), p. 115

van Ballegooijen, A. A., & Hasan, S. S. 2003, in *Current Theoretical Models and High Resolution Solar Observations: Preparing for ATST*, eds. A. A. Pevtsov, & H. Uitenbroek, ASP Conf. Series, Vol. 286, p.155

van Ballegooijen, A. A., Nisenson, P., Noyes, R. W., Löfdahl, M. G., Stein, R. F., Nordlund, Å., & Krishnakumar, V. 1998, ApJ, 509, 435

van Ballegooijen, A. A., Asgari-Targhi, M., & Berger, M. A. 2014, ApJ, 787, 87

van Ballegooijen, A. A., Asgari-Targhi, M., Cranmer, S. R., & DeLuca, E. E. 2011, ApJ, 736, article 3 (paper I)

van Ballegooijen, A. A., & Asgari-Targhi, M. 2016, ApJ, 821, 106

van Ballegooijen, A. A., & Asgari-Targhi, M. 2017, ApJ, 835, 10 (paper V)

Verdini, A., & Velli, M. 2007, ApJ, 662, 669

Viall, N. M., & Klimchuk, J. A. 2011, ApJ, 738, 24

Viall, N. M., & Klimchuk, J. A. 2012, ApJ, 753, 35

Vigeesh, G., Fedun, V., Hasan, S. S., & Erdélyi, R. 2012, ApJ, 755, 18

Wentzel, D. G. 1974, SoPh, 39, 129

Wang, H. 1988, SoPh, 116, 1

Warren, H. P., Winebarger, A. R., Mariska, J. T., Doschek, G. A., & Hara, H. 2008, ApJ, 677, 1395

Warren, H. P., Brooks, D. H., & Winebarger, A. R. 2011, ApJ, 734, 90

Warren, H. P., Winebarger, A. R., & Brooks, D. H. 2012, ApJ, 759, 141

Wedemeyer-Böhm, S., Scullion, E. Steiner, O., et al. 2012, Nature, 486, 505

Winebarger, A. R., Schmelz, J. T., Warren, H. P., Saar, S. H., & Kashyap, V. L. 2011, ApJ, 740, 2

Wilmot-Smith, A. L., Hornig, G., & Pontin, D. I. 2009, ApJ, 704, 1288

Wilmot-Smith, A. L. 2015, Phil. Trans. R. Soc. A 373, 20140265, http://dx/doi.org/10.1098/rsta.2014.0265

Yelles Chaouche, L., Solanki, S. K., & Schüssler, M. 2009, A&A, 504, 595

Young, P. R., Del Zanna, G., Mason, H. E., et al. 2007, PASJ, 59, S857

Zhang, J., White, S. M., & Kundu, M. R. 1998, ApJL, 504, L127

Zirker, J. B. 1993, SoPh, 148, 43